Shear thinning near the critical point of xenon

Robert F. Berg and Michael R. Moldover
National Institute of Standards and Technology, Gaithersburg, Maryland 20899, USA

Minwu Yao
Ohio Aerospace Institute, Cleveland, Ohio 44142, USA

Gregory A. Zimmerli
NASA Glenn Research Center, Cleveland, Ohio 44135, USA

(Received 27 September 2007; revised manuscript received 31 January 2008; published 17 April 2008)

We measured shear thinning, a viscosity decrease ordinarily associated with complex liquids, near the critical point of xenon. The data span a wide range of reduced shear rate: $10^{-3}<\dot{\gamma}\tau<700$, where $\dot{\gamma}\tau$ is the shear rate scaled by the relaxation time τ of critical fluctuations. The measurements had a temperature resolution of 0.01 mK and were conducted in microgravity aboard the Space Shuttle Columbia to avoid the density stratification caused by Earth's gravity. The viscometer measured the drag on a delicate nickel screen as it oscillated in the xenon at amplitudes $3\ \mu\mathrm{m}<x_0<430\ \mu\mathrm{m}$ and frequencies $1\ \mathrm{Hz}<\omega/2\pi<5\ \mathrm{Hz}$. To separate shear thinning from other nonlinearities, we computed the ratio of the viscous force on the screen at $\dot{\gamma}\tau$ to the force at $\dot{\gamma}\tau\approx 0$: $C_\gamma \equiv F(x_0,\omega\tau,\dot{\gamma}\tau)/F(x_0,\omega\tau,0)$. At low frequencies, $(\omega\tau)^2<\dot{\gamma}\tau$, C_γ depends only on $\dot{\gamma}\tau$, as predicted by dynamic critical scaling. At high frequencies, $(\omega\tau)^2>\dot{\gamma}\tau$, C_γ depends also on both x_0 and ω. The data were compared with numerical calculations based on the Carreau-Yasuda relation for complex fluids: $\eta(\dot{\gamma})/\eta(0)=[1+A_\gamma|\dot{\gamma}\tau|]^{-x_\eta/(3+x_\eta)}$, where $x_\eta=0.069$ is the critical exponent for viscosity and mode-coupling theory predicts $A_\gamma=0.121$. For xenon we find $A_\gamma=0.137\pm0.029$, in agreement with the mode coupling value. Remarkably, the xenon data close to the critical temperature T_c were independent of the cooling rate (both above and below T_c) and these data were symmetric about T_c to within a temperature scale factor. The scale factors for the magnitude of the oscillator's response differed from those for the oscillator's phase; this suggests that the surface tension of the two-phase domains affected the drag on the screen below T_c.

DOI: 10.1103/PhysRevE.77.041116 PACS number(s): 64.60.Ht, 83.10.Gr, 83.60.Df, 83.60.Fg

I. INTRODUCTION

Both oil in a car engine and paint on a paintbrush need viscosity control. Sliding engine parts sometimes shear the intervening oil layer fast enough to decrease the viscosity of the oil's polymer additives, and such *shear thinning* is bad for the engine. Conversely, brushing a well-engineered paint onto a wall temporarily decreases the paint's viscosity, and shear thinning helps spread the paint. In general, shearing any fluid fast enough to distort its microscopic structure will change the viscosity. Shear thinning, a decrease in viscosity with increasing shear rate, is common in complex fluids from molten plastics to ketchup; such fluids have microscopic structures that relax slowly in comparison with the shear rate $\dot{\gamma}$.

Here, we report the observation of shear thinning in the monatomic fluid xenon. A viscometer measured the drag on a delicate nickel screen as it oscillated in a sample of xenon at its critical density ($\rho_c=1.1\ \mathrm{g/cm^3}$). Upon approaching the liquid-vapor critical temperature ($T_c=17\ ^\circ\mathrm{C}$), the relaxation time τ of the critical fluctuations increased by orders of magnitude and shear thinning occurred when $\dot{\gamma}\tau>1$. The critical fluctuations have a size ξ that increases as a fluid approaches its liquid-vapor critical point. Coupling between fluctuations of density and velocity causes the viscosity η to increase as the power law $\eta\propto\xi^{x_\eta}$ [1,2]. The viscosity increase is small because the universal exponent $x_\eta=0.069$ is small [3,4]. However, the fluctuation relaxation time τ has the much stronger increase,

$$\tau=\tau_0\left(\frac{T-T_c}{T_c}\right)^{-1.93}\propto\xi^{3+x_\eta}, \tag{1}$$

as the temperature T approaches the critical temperature T_c [2].

Although the time constant amplitude τ_0 in Eq. (1) is tiny (1 ps), we achieved a relaxation time as large as $\tau=1$ s during the microgravity measurements by operating within 1 mK of the critical temperature. In addition to microkelvin temperature control, the viscometer had better than 0.1% viscosity resolution at low frequencies because the screen's small mass (1 mg) made the viscometer insensitive to vibrations of the space shuttle's structure.

Shear thinning occurs when the shear rate $\dot{\gamma}$ exceeded $1/\tau$. A related phenomenon, viscoelasticity, occurs at small shear rates when the shearing is oscillatory at a frequency f that exceeds $1/\tau$. The first accurate measurement of near-critical viscoelasticity was made by a previous microgravity experiment CVX (Critical Viscosity of Xenon) [3]. The present experiment, CVX-2, measured shear thinning by driving the same viscometer to amplitudes 30 times larger. Specifically, the viscometer measured the amplitude and phase of the hydrodynamic force $F(x_0,f,\dot{\gamma}\tau)$ on the nickel screen as it was driven through the xenon at several amplitudes ($3\ \mu\mathrm{m}<x_0<430\ \mu\mathrm{m}$) and frequencies ($1\ \mathrm{Hz}<f<5\ \mathrm{Hz}$). To separate the $\dot{\gamma}\tau$ dependence of the force from the frequency and amplitude dependences, we computed the ratio

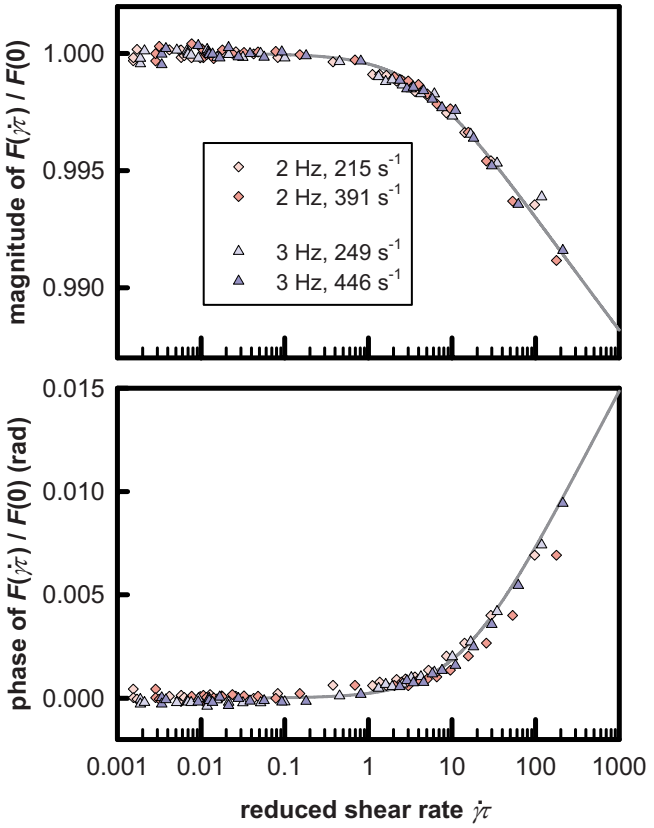

FIG. 1. (Color online) Magnitude and phase of the hydrodynamic force on the tip wire of the viscometer at different shear rates. The data (run 4) are normalized by the force expected in the absence of shear thinning. [See Eq. (19).] The curves are empirical functions [Eq. (20a) and (20b)] fitted to the 3-Hz data. Two drive torques were used for both frequencies, and the points are labeled by the maximum shear rate (s^{-1}) at the surface of the oscillator. (See Table I.)

$$C_\gamma \equiv F(x_0,f,\dot{\gamma}\tau)/F(x_0,f,0). \tag{2}$$

Shear thinning caused the values of C_γ to depend on $\dot{\gamma}\tau$, as shown in Fig. 1 for measurements at 2 Hz and 3 Hz.

The density of a fluid near its liquid-vapor critical point is enormously sensitive to gradients of pressure and temperature. Shear thinning cannot be observed in quiescent xenon on Earth because the gradient of pressure caused by Earth's gravity stratifies the density so that the layer near critical density is too thin to be studied in a viscometer. To reduce gravitational stratification, the measurements were conducted in microgravity aboard the Space Shuttle Columbia in 2003 during the ill-fated mission STS-107. Much of the data were downlinked during the flight, and the unexpected recovery of the hard disk drive from Columbia's debris made 99% of the data available.

One could reduce the stratification on Earth by operating the viscometer farther from T_c—say, at T_c+90 mK. However, the fluctuation decay time would then be only 7 μs and achieving $\dot{\gamma}\tau=100$ would require a viscous heating per unit volume as large as $\eta\dot{\gamma}^2/2=6$ kW cm^{-3}. In contrast,

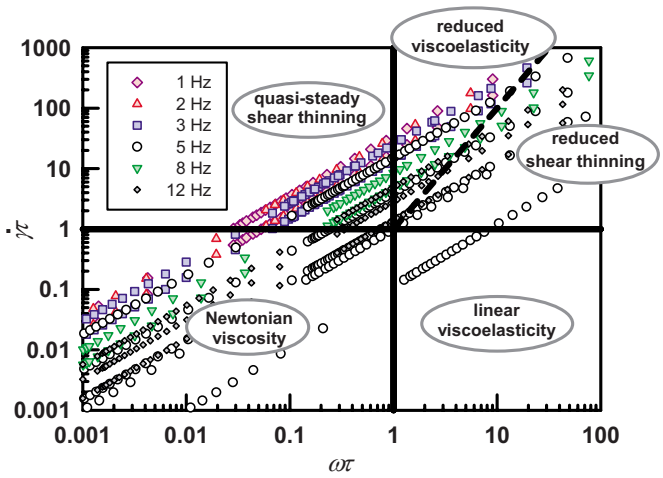

FIG. 2. (Color online) The experimental data spanned regions of Newtonian viscosity $(1>\omega t,\dot{\gamma}t)$, linear viscoelasticity $(\omega\tau>1>\dot{\gamma}\tau)$, quasisteady shear thinning $(\dot{\gamma}\tau>1>\omega\tau)$, reduced shear thinning $(\omega\tau>\dot{\gamma}\tau>1)$, and reduced viscoelasticity $(\dot{\gamma}\tau>\omega\tau>1)$. The diagonal dividing line is the inequality $(\omega\tau)^2<\dot{\gamma}\tau$ discussed in Sec. VII F.

the present experiment achieved $\dot{\gamma}\tau=100$ with less than 0.2 mW/cm^{-3}. (The total heating at the largest amplitudes was 7 μW.)

The flow near each wire making up the oscillating screen was approximately that caused by a cylinder oscillating transversely to its axis. The lack of a steady, uniform shear field complicated the analysis in two ways. First, the oscillator's deviation from linear force-vs-velocity behavior at large amplitudes was primarily due to inertia (the convective term in the Navier-Stokes equation) instead of shear thinning. To deal with this complication we carefully studied the oscillator's hydrodynamics on Earth while the viscosity was Newtonian [5]. Second, the oscillator's response was affected by viscoelasticity $(f\tau>1)$ as well as shear thinning $(\dot{\gamma}\tau>1)$. Understanding their combined effects requires a comprehensive constitutive relation, but no appropriate theory for the near-critical rheology of xenon exists. Therefore, we analyzed our data using the theory for shear thinning at zero frequency, recognizing that this is an approximation.

Figure 2 shows the wide range of reduced frequency $\omega\tau$ and shear rate $\dot{\gamma}\tau$ of the present measurements. The plot is divided into five regions corresponding to the five combinations of $\omega\tau$ and $\dot{\gamma}\tau$ discussed in the next section. Significant data were collected in all five regions. (The reference data at small shear rates, much of which would fall into the linear viscoelasticity region, are not shown.)

Capillary viscometers have been used to observe shear thinning near the consolute points of binary liquid mixtures [6–12]. The measurement of Hamano *et al.* near the consolute point of a micellar solution is particularly valuable because it used a Couette viscometer to create a uniform shear field [13]. Their results are described by [14]

$$\frac{\eta(\dot{\gamma}\tau)}{\eta(0)} = [1 + A_\gamma|\dot{\gamma}\tau|]^{-p}, \tag{3}$$

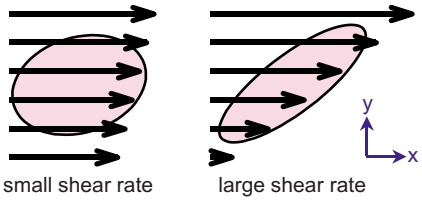

FIG. 3. (Color online) Simple flow fields with small and large shear rates. By imagining a critical fluctuation as a spherical droplet cluster, we illustrate how the shear field distorts the shapes of fluctuations.

where the theoretical exponent is $p \equiv x_\eta/(3+x_\eta)=0.0225$. Oxtoby's mode-coupling prediction for the shear-rate scale factor is $A_\gamma=0.121$ [15]. (The definition of A_γ differs here from that used in [14]. In that article, the theoretical shear-rate scale factor was defined as bA_γ, with $b=0.121$ and $A_\gamma \equiv 1$ for theory.) The experimental value from the micellar solution of Hamano *et al.* is $A_\gamma = 0.067 \pm 0.012$, which disagrees with our present result for xenon of $A_\gamma=0.137 \pm 0.029$. [The uncertainty for the micellar solution includes the 10% uncertainty from fitting Eq. (3) [14] plus the 14% uncertainty of τ due to the correlation length [16]. The uncertainty of the present result is discussed in Sec. VII G.] Shear thinning near critical points, though tiny, is important because the underlying theory seems capable of providing a comprehensive constitutive relation without detailed knowledge of the intermolecular interactions. The only example of a similarly close tie between experiment and theory for noncritical fluids is work by Bair *et al.*, who observed shear thinning in a pure liquid, squalane ($C_{30}H_{62}$), at ~1 GPa [17]. Fluctuations were negligible because the squalane was far from its critical point, but shear thinning occurred because, at 1 GPa, the molecular rotation time increased to approximately 0.01 s. They found a remarkable agreement between their measurements and their nonequilibrium molecular dynamics calculations. Unlike the present work, the calculations required a description of the molecule and the experimental analysis required a time-temperature superposition of the sort often used by polymer scientists to correlate polymer data [18].

The rest of the paper is organized as follows. Section II summarizes the theory. Section III describes the experimental apparatus. Section IV discusses the hydrodynamics of the oscillator. Section V describes the experimental methods. Section VI describes the reduction of the experimental data. Section VII describes the experimental results, which include the observation of an effective viscosity below T_c, a lack of evidence for normal stress, scaling of the data with reduced shear rate, and failure of that scaling at large reduced frequency. The appendixes include calculations of the shear rate (Appendix A), an estimate of how shear thinning reduces the force on an oscillating cylinder (Appendix B), and tables of experimental data (Appendix C).

II. THEORY

A complete understanding of the rheology of any fluid must include its constitutive relation, the simplest of which is

$$\sigma_{xy} = -\eta \frac{dv_x}{dy} \equiv -\eta\dot{\gamma}_{xy}. \tag{4}$$

Equation (4) relates the xy component of the stress tensor σ to the xy component of the shear rate tensor $\dot{\gamma}$ via the viscosity η. It applies to the simple flow field of Fig. 3, for which $v_x=\dot{\gamma}y$ and $v_y=v_z=0$.

Equation (4) describes a *Newtonian* fluid. In addition to the viscosity divergence, theory predicts that near-critical fluids are *non-Newtonian*: the value of the viscosity η depends on the shear rate $\dot{\gamma}$ [15,19,20]. Reviews of transport properties near critical points [1,2,21–24] lack detailed discussions of near-critical rheology; of more relevance here are the focused papers by Bhattacharjee and Ferrell on viscoelasticity [25], Oxtoby [15] and Das and Bhattacharjee [20] on shear thinning, and Onuki and Kawasaki on normal stress [26]. Sections II A–II C discuss these phenomena individually. Section II D discusses the combination of viscoelasticity and shear thinning, which occurred in the CVX-2 experiment.

We find it useful to imagine a typical critical fluctuation as a spherical droplet cluster of size ξ and lifetime τ, as suggested by Fig. 3. More realistic models have used fractal droplet clusters with a distribution of sizes to understand dynamic critical phenomena [27–30].

A. Viscoelasticity

Viscoelasticity occurs when a fluid's microscopic structure is sheared at a frequency f that exceeds the inverse of the structure's decay time τ, so that $f\tau>1$. In the droplet cluster diagram of Fig. 3, the shear field increases the cluster's energy by increasing its interfacial area. If the shear direction is reversed before the cluster decays, some of the extra energy is recovered and viscoelasticity occurs. If the distortion of the cluster is small, the fluid response is proportional to the shear rate and the resulting *linear viscoelasticity* can be described by generalizing the viscosity to a complex function of frequency. Figure 4 shows the good agreement between the low-shear-rate results from CVX [3] and Bhattacharjee and Ferrell's theory for viscoelasticity [25]. The curves represent the theoretical expression for the complex viscosity,

$$\eta(\omega\tau) = \eta(0)[S(A_\omega z)]^{-p}, \tag{5}$$

with $A_\omega=2.0$. The frequency dependence of the scaling function $S(A_\omega z)$ is contained in the dimensionless argument $z \equiv i\omega\tau/2$, where ω is the angular frequency. [References [3] and [14] give $S(A_\omega z)$ with corrections of two typographic errors that appeared in [25].] The parameter A_ω allows for deviation from Bhattacharjee and Ferrell's original theory, for which $A_\omega \equiv 1$. An improved calculation by Das and Bhattacharjee [31] gave the theoretical value $A_\omega=1.4$.

B. Shear thinning and the Cox-Merz rule

Shear thinning occurs when the shear rate $\dot{\gamma}$ is large enough to distort the fluctuation during its lifetime τ, specifically $\dot{\gamma}\tau>1$. The fluid properties change because the distor-

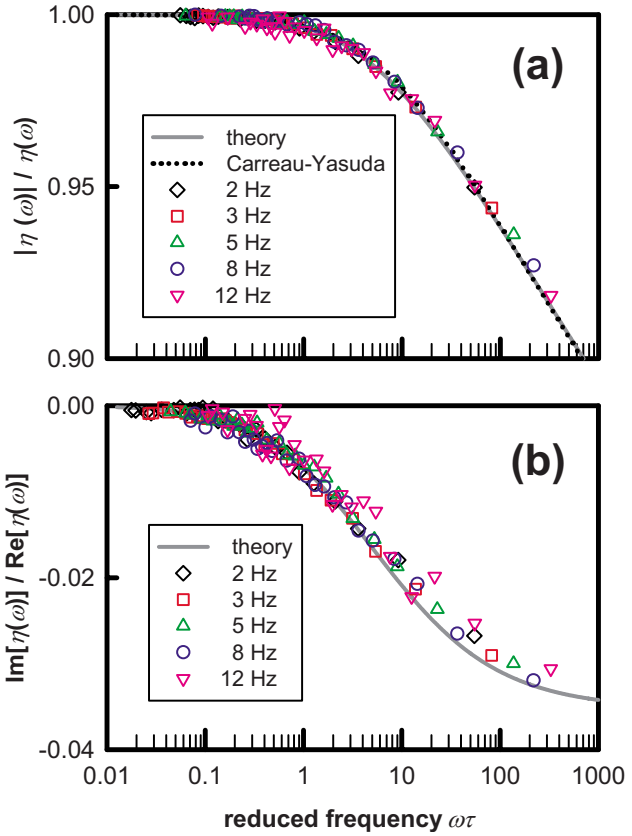

FIG. 4. (Color online) Viscoelasticity measured in xenon at critical density at frequencies from 2 to 12 Hz at small shear rates ($<10\ s^{-1}$) [3]. The solid curves resulted from fitting Eq. (5) to the data in the range $10^{-6}<\varepsilon<10^{-4}$. (a) The normalized viscosity magnitude $|\eta(\omega)|/\eta(0)$. The empirical Carreau-Yasuda relation [Eq. (3)] with $A_\gamma=0.157$ describes the data as well as the theory; this similarity of viscoelasticity and shear thinning, in which ω is substituted for $\dot{\gamma}$ according to Eq. (7), is known as the Cox-Merz rule. (b) The ratio $\mathrm{Im}(\eta)/\mathrm{Re}(\eta)$.

tion depicted on the right-hand side of Fig. 3 shortens the fluctuation's diffusive decay time and makes the fluid anisotropic.

In contrast to the theory for viscoelasticity, there is no published closed-form theoretical expression for shear thinning at intermediate values of $\dot{\gamma}\tau$. Oxtoby's mode-coupling calculations [15] produced a set of numerical results for $\eta(\dot{\gamma}\tau)$, and an analogy between the rheology of near-critical fluids and that of polymer fluids makes it possible to generalize those results to the useful expression (3). The analogy was provided by Douglas [32], who pointed out that, for near-critical fluids in the limits of small and large $\dot{\gamma}\tau$, results from renormalization group theory are consistent with the Carreau-Yasuda relation [33–35] that describes the shear thinning of many polymer fluids. Equation (3) is a slight improvement over Douglas' expression, which assumed that the reduced shear rate entered Eq. (3) as $(\dot{\gamma}\tau)^2$ instead of the nonanalytic form $|\dot{\gamma}\tau|$.

The same renormalization group theory also predicts that a shear rate $\dot{\gamma}$ will shift the critical temperature by the amount [36]

$$[T_c(\dot{\gamma})-T_c(0)]=-s(4-d)T_c(0)(\tau_0\dot{\gamma})^{0.517}, \tag{6}$$

where $s=0.0832$ and $d=3$ is the number of spatial dimensions. In spite of this shift, the temperature-dependent time constant τ in Eq. (3) should be identified with the order parameter relaxation time in the absence of shear [37,38]. This is required for consistency with the renormalization group calculations, which were carried out only to first order in the expansion perturbation parameter $4-d$ [e.g., see Eq. (6)]. In particular, the coefficient A_γ in Eq. (3) must vanish in the limit $4-d\to 0$, and consistency in Eq. (3) to first order in $4-d$ makes it appropriate to identify τ with its *unsheared* fluid value [38]. Thus, we do not consider τ itself to depend on shear rate, which simplifies our analysis considerably.

Remarkably, Eq. (3) describes also the magnitude of the complex viscosity. Figure 4 shows that the choice $A_\gamma=0.157$ makes Eq. (3) indistinguishable from the experimental data and the theoretical magnitude obtained from Eq. (5). Polymer fluids that have such a similarity between shear thinning and viscoelasticity are said to obey the Cox-Merz rule, which is often used to estimate the shear thinning of polymer melts [18,39]. The empirical Cox-Merz rule [40] equates the viscosity $\eta(\dot{\gamma})$ measured at shear rate $\dot{\gamma}$ in the limit of small frequency with the magnitude of the complex viscosity $\eta(\omega)$ measured at frequency ω in the limit of small shear rate. A slightly generalized form of the rule,

$$\eta(k_{\mathrm{CM}}\dot{\gamma})=|\eta(\omega)|_{\omega=\dot{\gamma}}, \tag{7}$$

with $k_{\mathrm{CM}}\sim 1$, apparently holds near the critical point of simple fluids as well [14]. The validity of the Cox-Merz rule strengthens the analogy between polymer fluids and near-critical fluids, and it supports the use of Eq. (3) to describe near-critical shear thinning.

C. Normal stress difference

In addition to the shear stress σ_{xy}, a non-Newtonian liquid can support stresses normal to the flow direction. Figure 3 suggests how the quantity $\sigma_{xx}-\sigma_{yy}$, known as the first normal stress difference by rheologists, can arise. If the fluid is viscoelastic, a restoring force will impart a tension to the entire fluid in the x direction as well as oppose the stretching of an individual fluctuation.

Onuki and Kawasaki [26] estimated the following limiting values for the first normal stress difference in a near-critical fluid:

$$\frac{\sigma_{xx}-\sigma_{yy}}{\sigma_{xy}}\approx 0.02\dot{\gamma}\tau, \quad \dot{\gamma}\tau\ll 1,$$

$$\frac{\sigma_{xx}-\sigma_{yy}}{\sigma_{xy}}\approx 0.046, \quad \dot{\gamma}\tau\gg 1. \tag{8}$$

A simple formula that interpolates between these limits is

$$\frac{\sigma_{xx}-\sigma_{yy}}{\sigma_{xy}}=\frac{S_\infty|\dot{\gamma}\tau|}{|\dot{\gamma}\tau|_0+|\dot{\gamma}\tau|}, \tag{9}$$

where $S_\infty=0.046$ and $|\dot{\gamma}\tau|_0=2.3$.

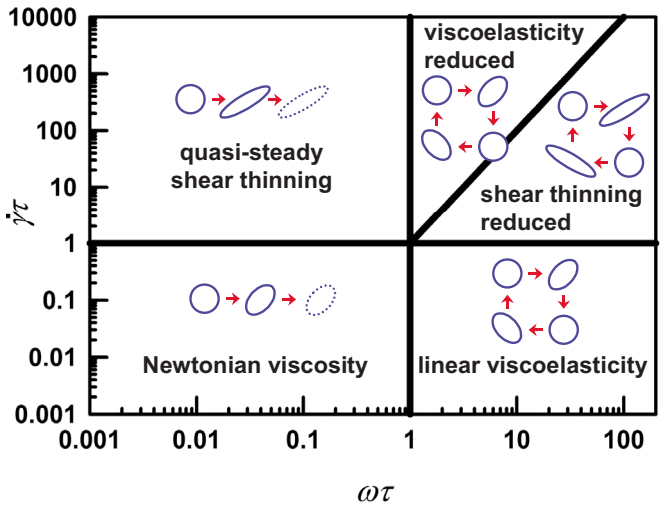

FIG. 5. (Color online) Five possible combinations of reduced frequency $\omega\tau$ and reduced shear rate $\dot{\gamma}\tau$ and their influence on the evolution of a fluctuation during its lifetime τ. The diagonal line that divides the region of large shear rate and frequency is Eq. (32).

D. Viscoelasticity and shear thinning combined

The oscillator's response was affected simultaneously by viscoelasticity ($f\tau > 1$) and shear thinning ($\dot{\gamma}\tau > 1$), so we approximated xenon's rheology as the following product of viscoelasticity in the limit of zero shear rate [Eq. (5)] and shear thinning in the limit of zero frequency [Eq. (3)]:

$$\eta(\omega\tau, \dot{\gamma}\tau) \simeq \eta(0,0)[S(iA_\omega\omega\tau/2)]^{-p}[1 + A_\gamma|\dot{\gamma}\tau|]^{-p}. \quad (10)$$

This approximation is an example of a "generalized Newtonian fluid" [18], which assumes only that the viscosity depends on the shear rate. It failed when both the frequency and shear rate were large. To gain some understanding of the failure of Eq. (10), we divided the experimental conditions into the five following possible combinations of reduced frequency and shear rate.

(i) $1 > \omega\tau, \dot{\gamma}\tau$, *Newtonian viscosity.* The frequency and shear rate are both small. The fluctuation has only a small distortion when it disappears.

(ii) $\dot{\gamma}\tau > 1 > \omega\tau$, *quasisteady shear thinning.* The frequency is small but the shear rate is large. The fluctuation distorts significantly before it disappears, which causes shear thinning.

(iii) $\omega\tau > 1 > \dot{\gamma}\tau$, *linear viscoelasticity.* The frequency is large but the shear rate is small. The small distortion makes the fluid response proportional to the shear rate, and its recovery causes viscoelasticity.

(iv) $\omega\tau > \dot{\gamma}\tau > 1$, *reduced shear thinning.* Both frequency and shear rate are large. Reversal of the shear rate keeps the distortion small and suppresses shear thinning.

(v) $\dot{\gamma}\tau > \omega\tau > 1$, *reduced viscoelasticity.* Both frequency and shear rate are large. Distortion of the fluctuation shortens its lifetime and suppresses viscoelasticity.

Figure 5 depicts how each of the five combinations might affect the evolution of a fluctuation during its lifetime. All five combinations occurred in the CVX-2 experiment, and this pictorial reasoning provided a qualitative understanding of the present results.

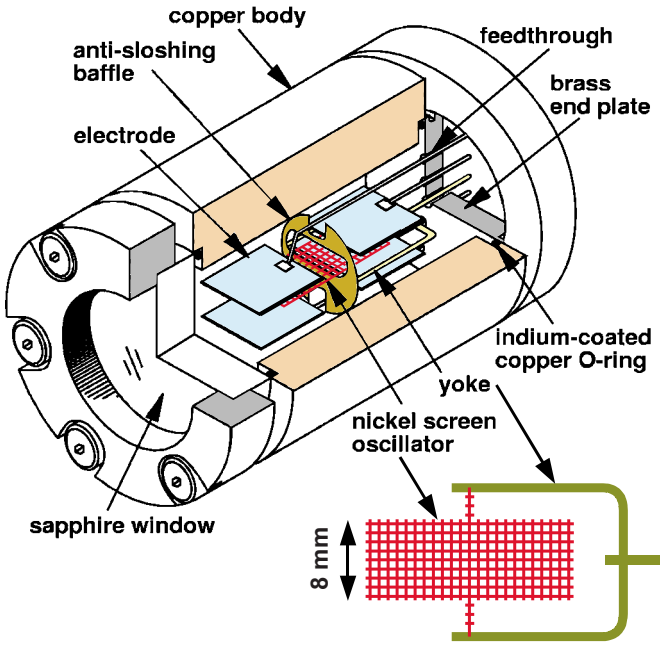

FIG. 6. (Color online) Cutaway view of the viscometer cell. The cylindrical volume occupied by the xenon was 38 mm long and 19 mm in diameter. Torque was applied to the screen by applying different voltages to diagonal pairs of electrodes while maintaining the screen at ground potential.

Das and Bhattacharjee recently derived an expression for the combined effects of viscoelasticity and shear thinning [20]; their Eq. (22) can be written in terms of reduced frequency and shear rate as follows:

$$\eta(\omega\tau, \dot{\gamma}\tau) = \eta(0,0)[S(iA_\omega\omega\tau/2)]^{-p} \times \left[1 + (A_\gamma\dot{\gamma}\tau)^{1/2}\frac{[1 + 2.5(1-i)(\omega\tau)^{1/2}]}{[1 - (i/2)(\omega\tau)]}\right]^{-2p}. \quad (11)$$

(Das and Bhattacharjee's value for the shear-rate scale factor is $A_\gamma = 0.09$.) At small frequencies $\omega\tau \ll 1$, Eq. (11) is identical to the approximate equation (10) in the limits of zero shear rate and very large shear rates, yielding, respectively, viscoelasticity without shear thinning and $\eta \propto (A_\gamma\dot{\gamma}\tau)^{-p}$. At large frequencies $\omega\tau \gg 1$, Eq. (11) predicts that the shear thinning will saturate at a constant value that depends on the dimensionless ratio $\omega/\dot{\gamma}$. This is expected from the pictorial reasoning above, and it agrees qualitatively with the experimental results discussed in Sec. VII F.

However, Eq. (11) was not used to analyze the experimental data for two reasons. First, at intermediate shear rates, Eq. (11) is proportional to $[1 + (A_\gamma\dot{\gamma}\tau)^{1/2}]^{-2p}$, which differs significantly from the form of Eq. (3) that describes Oxtoby's calculations as well as the measured viscoelasticity of xenon (as suggested by the Cox-Merz rule). Second, Eq. (11) predicts that, for $\omega\tau < 1$, increasing the frequency at fixed reduced shear rate will initially increase the shear thinning, but no such behavior was seen in the present results.

III. APPARATUS

A. Xenon sample and the immersed oscillator

The xenon sample in the sealed cell was the same one that we used for the CVX experiment [3]. It had an average density $\langle\rho\rangle=(0.9985\pm0.0017)\rho_c$, where ρ_c is the critical density. The density was deduced from the height of the liquid-vapor meniscus when the sample was in equilibrium a few millikelvin below T_c. The weights of the sample cell in 1996 (before CVX) and in 1998 (after CVX) differed by less than 0.02% of the sample mass; extrapolating this bound on the leak rate implies a xenon loss of less than 0.06% between the dates of CVX and CVX-2. As T_c was approached during CVX-2, the low-frequency, low-shear-rate viscosity increased exactly as it did during CVX. Seven months after the Columbia disaster in 2003, the meniscus height was remeasured in the recovered sample cell, showing that $\langle\rho\rangle=(1.000\pm0.003)\rho_c$.

Figure 6 displays the viscometer in the sample cell. The oscillator was an 8 mm $\times$ 19 mm rectangle of nickel screen that had been cut out of a larger piece of screen. The screen consisted of a square grid of "wires" formed by electrodeposition. When the screen was cut, one wire was left extending from the middle of both of the rectangle's long edges. These two extensions were soldered to a stiff yoke to act as torsion springs. The yoke supported the screen between four electrodes placed parallel to the screen. Oscillating voltages applied to the electrodes generated an oscillating torque on the screen, which caused it to oscillate much like a child's seesaw. A more detailed description of the cell appears in [3].

In 2000, between CVX and CVX-2, we measured the oscillator's response as defined by Eq. (14). The response measured in 2000 had a small, frequency-dependent difference from the response measured before CVX in 1997. The difference ($\leq$0.4% in magnitude and $\leq$3 mrad in phase) was small enough to be ignored because it was consistent with the unimportant drag of a small (30 μm $\times$ 300 μm) dust particle adhering to the screen.

B. Drive and detection electronics

Here, we emphasize the features of the electronics that were new or important to the operation of CVX-2. Details in common with CVX can be found in [3]. To measure shear thinning, the oscillator was driven electrostatically at a frequency from 0.5 Hz to 12 Hz. Two square-root amplifiers combined a dc voltage $V_{\rm dc}$ with a sinusoidal voltage $V_{\rm in}(t)=V_0\cos(\omega t)$, and their complementary outputs were applied to the two electrode pairs surrounding the oscillator. The resulting dimensionless torque on the oscillator was

$$N(t)=K_{\rm torque}\left[\frac{V_{\rm in}(t)}{V_{\rm dc}}+\frac{x_{\rm tip}(t)}{x_{\rm gap}}\right], \tag{12}$$

where $x_{\rm tip}(t)$ is the displacement at the oscillator's tip and $x_{\rm gap}\approx4$ mm is the length of the gap between the oscillator and one electrode. The dimensionless calibration factor $K_{\rm torque}$ was adjusted so that the values of dimensionless torque obtained for small amplitude [$B(R/\delta)$ in Eq. (15)] agreed with those determined earlier for the CVX experiment [3], which also were made at small amplitude.

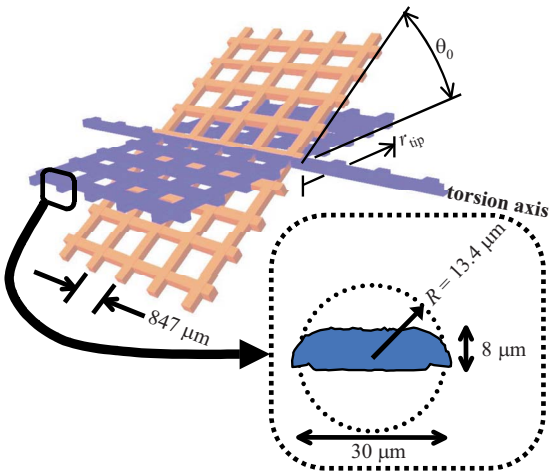

FIG. 7. (Color online) Schematic diagram of the oscillator (not to scale). The oscillator's angular displacement θ_0 generated the local displacement amplitude $x_0=r\theta_0$, where r is the distance from the torsion axis. The inset shows the cross section of a typical oscillator wire superposed on a circle of radius $R=13.4$ μm used in our CFD calculations.

During the first run of CVX-2 through T_c, the torque applied to the oscillator was a frequency chirp similar to that used by CVX, so that $V_{\rm in}(t)$ was proportional to a time-dependent voltage created by summing 400 equal-amplitude sine waves at frequencies spaced evenly between 0 Hz and 25 Hz. The voltages $V_{\rm dc}=30$ V and V_0 were the same small values used for CVX. Under these conditions, nonlinearity of the oscillator's response due to shear thinning and hydrodynamics was negligible. During subsequent runs through T_c, only single-frequency torques were applied. The dc voltage was increased to $V_{\rm dc}=75$ V and the ac amplitude V_0 was increased to create drive torques as much as 31 times larger than for CVX.

As a result of increasing $V_{\rm dc}$ and the oscillator displacement, the second term of Eq. (12) became much more significant. This term acts as a negative contribution to the oscillator's spring constant (electrostatic spring softening), and increasing $V_{\rm dc}$ from 30 V to 75 V decreased the oscillator's small-amplitude resonance frequency f_0 by approximately 1 Hz from its initial value of 11 Hz. Before filling the sample cell, we had measured f_0 in vacuum at $V_{\rm dc}=30$ V. To determine its value at $V_{\rm dc}=75$ V in the filled cell we modeled the ratio of the oscillator's frequency responses measured at 30 V and 75 V. Fitting the model to the response ratio yielded the value of the derivative $df_0/dV_{\rm dc}^2$, from which we calculated $f_0(75\ {\rm V})=f_0(30\ {\rm V})-(df_0/dV_{\rm dc}^2)[(75\ {\rm V})^2-(30\ {\rm V})^2]$. Terms of order $(x_{\rm tip}(t)/x_{\rm gap})^2$ and higher were not included in Eq. (12) because the oscillator's small amplitude and the approximate symmetry of the electrode pairs made them negligible.

The oscillator's time-dependent angular displacement $\theta(t)$ was detected by the unbalance of a capacitance bridge operating at 10 kHz. The out-of-balance signal was fed to a

TABLE I. CFD estimates of the maximum shear rate (in s^{-1}) at the surface of the experimental oscillator at $T_c+0.1$ mK.

Run	Frequency (Hz)	Torque relative to CVX				
		0.62 or 1.25	3.1	9.3	18.7	31.1
1	0.06–25 chirp	<12				
2	5	7	38	117		438
3	1	7		111		207
	3	15		249		446
	5	15		246		438
	8	14		223		392
4	2	13		215		391
	3	15		249		446
5	12	13		98	200	346

lock-in amplifier, which generated a voltage whose oscillating component $V_{out}(t)$ was proportional to $\theta(t)$:

$$\theta(t) = \theta_0 \cos(\omega t) = \frac{1}{r_{tip}}\left(\frac{dx_{tip}}{dV_{out}}\right)V_{out}(t). \tag{13}$$

Here r_{tip} is the distance from the torsion axis to the oscillator's tip. (See also Fig. 7.)

The oscillator's response was defined as the Fourier transform $\hat{\theta}(f)$ of the angular displacement divided by the Fourier transform $\hat{N}(f)$ of the applied torque:

$$G(f,\theta_0) = \frac{\hat{\theta}(f)}{\hat{N}(f)} = \frac{K}{r_{tip}}\left(\frac{dx_{tip}}{dV_{out}}\right)\frac{\hat{V}_{out}(f)}{\hat{V}_{in}(f)}. \tag{14}$$

Here $\hat{V}_{in}(f)$ and $\hat{V}_{out}(f)$ are the Fourier transforms of the input and output voltages.

The amplitude V_0 and frequency f of the ac drive voltage determined the oscillation amplitude x_0. A determination of the hydrodynamic force at amplitude x_0 comprised at least two measurements. The first measurement used a torque amplitude that was sufficiently small to make negligible nonlinearity due to hydrodynamics and shear thinning. (See Table I.) The other measurements used larger torques to drive the oscillator at amplitude x_0.

Changes to the CVX electronics included programmable drive voltages (V_{dc} and V_0), a power amplifier that allowed larger drive torques, and a variable-gain preamplifier that increased the lock-in amplifier's input range by a factor of 10.

C. Thermostat and flight canisters

The flight instrument was contained in two sealed aluminum "Hitchhiker" canisters connected to one another by a power-communications cable. During the first 2 days, the lid of the canister that contained the thermostat cooled from 18 °C to 11 °C. Afterwards, except for brief periods when the space shuttle payload bay was oriented toward the sun, it remained at 11.0 ± 0.3 °C.

The flight canisters, thermostat, and electronics used for control of the sample temperature were the same as those used for CVX. Maintaining adequate sample homogeneity near T_c required that temperature differences within the sample be less than 0.2 μK. The thermostat comprised three coaxial aluminum shells surrounding the thick-walled copper sample cell. The thermostat's response time was long, approximately 1 h, but much less than the sample's internal response time near the critical point. Sensitive measurements of temperature differences in a test thermostat [41] verified that the thermostat could achieve such small temperature differences. The CVX and CVX-2 measurements were independent of the sample's temperature history, which is evidence that the density and temperature of the xenon in the vicinity of the oscillator were adequately controlled. The thermostat's construction and operation are described in more detail elsewhere [3,41].

IV. HYDRODYNAMICS OF THE OSCILLATOR

A. Newtonian hydrodynamics of a cylinder oscillating at large amplitude

We modeled the oscillator as an assembly of isolated cylinders of noncircular cross section, each oscillating transversely to its axis at an amplitude proportional to its distance from the torsion axis. Because the angular amplitude of the oscillator was small ($\theta_0 < 0.05$ rad), we could approximate each cylinder's motion as a linear displacement $x(t) = \mathrm{Re}[x_0 e^{i\omega t}]$, where x_0 is the displacement amplitude.

If x_0 is sufficiently small, the hydrodynamic force $F(t)$ exerted on a unit length of a cylinder will be periodic and proportional to x_0. The proportionality allows $F(t)$ to be written as the product of the fluid mass per unit length displaced by the cylinder ($\pi R^2 \rho$, where R is the cylinder's effective radius and ρ is the fluid density), the cylinder's acceleration amplitude ($\omega^2 x_0$, where $\omega = 2\pi f$), and a dimensionless reduced force $B(R/\delta)$ as follows [3]:

$$F(t) = \mathrm{Re}[\hat{F}_{small}(f)e^{i\omega t}] = \mathrm{Re}[-i(\pi R^2 \rho \omega^2 x_0)B(R/\delta)e^{i\omega t}]. \tag{15}$$

Here, the complex force amplitude is

$$\hat{F}_{small}(f) = \frac{1}{2\pi}\int_{-\infty}^{+\infty} F(t)e^{-i\omega t}dt, \tag{16}$$

and the viscous penetration length is defined by

$$\delta = \sqrt{\frac{2\eta}{\rho\omega}}. \tag{17}$$

Equation (15) is useful for calibrating an oscillator used as a viscometer because δ can be varied by changing the frequency while the oscillator is immersed in a fluid of known density and viscosity. Equation (15) applies to a cylinder of any cross section, and the choice of R used in $B(R/\delta)$ is arbitrary. Therefore, measuring the Fourier transform $\hat{F}_{small}(f)$ defined by Eq. (15) while varying the frequency yields the calibration function $B(R/\delta)$ without requiring knowledge of the oscillator's geometry.

The viscous penetration length was in the range 24 μm $< \delta <$ 190 μm. Thus δ was comparable to or larger than the

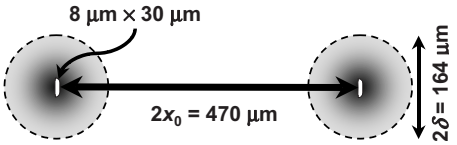

FIG. 8. Relative sizes of the oscillator wire cross section, viscous penetration depth δ, and oscillator amplitude x_0 at 3 Hz.

width of a screen wire (30 μm), but much less than the distance between wires (847 μm). Figure 7 shows that the cross section of a typical screen wire was approximately an 8 μm$\times$30 μm rectangle. Despite the wire's noncircular cross section, the drag on the screen at small displacement amplitudes has nearly the same functional form as that of an assembly of isolated cylinders of circular cross section [3,5].

For the larger amplitudes used by CVX-2, the drag was no longer proportional to x_0. Therefore we generalized Eq. (15) by multiplying the reduced force B by a complex function C that depends on reduced amplitude x_0/δ as well as R/δ:

$$\hat{F}(f) = \hat{F}_{\text{small}}(f) C\left(\frac{x_0}{\delta}, \frac{R}{\delta}\right). \tag{18}$$

Figure 8 shows the relative sizes of the oscillator wire cross section, viscous penetration depth, and oscillator amplitude when the viscometer was operated at maximum amplitude at 3 Hz.

We used computational fluid dynamics (CFD) to calculate the force on a circular cylinder oscillating transverse to its diameter in a Newtonian fluid. The motion was in the x direction with the assumption that the flow field was two-dimensional and symmetric about the x axis. In the CFD calculations, the values of the density and the viscosity were matched to the experimental conditions, and the cylinder radius was chosen to be 13.4 μm so that the calculated hydrodynamic force at small amplitude matched the measured value. The measured and the calculated values of C agreed, verifying the accuracy of the CFD results and the relevance of Eq. (18) in the range of x_0/δ and R/δ encountered in CVX-2 [3]. The calculations also showed that the dependence of C on R/δ is weak for the same ranges.

The CFD calculations also estimated the shear rate at the surface of the experimental oscillator. Figure 9 illustrates the dependence of the shear rate on position for three oscillation amplitudes. On the contours, the shear component of the rate-of-deformation tensor has constant values. At the largest amplitude, these contours and the shear field are asymmetric about the y axis. For simplicity, we characterized the shear rate by its maximum value $\dot{\gamma}_{\max}$ on the surface of the cylinder, as given by Eq. (A12) of Appendix A.

Table I lists the maximum shear rates calculated for a transversely oscillating circular cylinder with a radius of 13.4 μm.

B. Non-Newtonian hydrodynamics

In an attempt to understand the effect of near-critical shear thinning on the experimental oscillator, we used the Carreau-Yasuda relation [Eq. (3) with $A_\gamma \equiv 0.067$] in the CFD calculations. The CFD results agreed only qualitatively

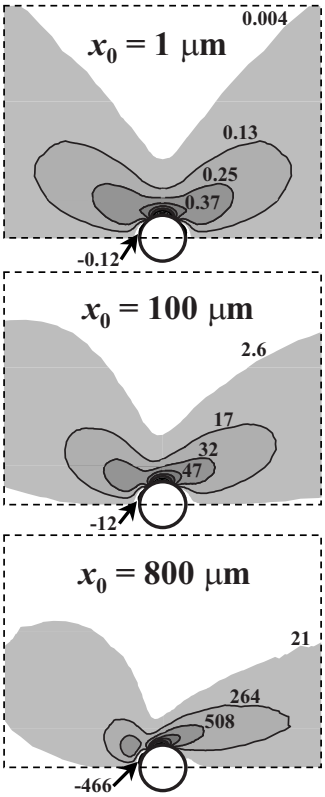

FIG. 9. Selected contours (in s^{-1}) of the shear component of the rate-of-deformation tensor D_{xy} near a cylinder oscillating at 5 Hz. The contours display the concentration of viscous stress near the cylinder when the cylinder moves from right to left at its maximum speed. Asymmetry is clearly visible at x_0=800 μm (x_0/δ=14.7). Negative values indicate shear rates of reversed direction; we characterized the shear rate field by its maximum magnitude.

with the experimental results, likely because the Carreau-Yasuda relation is not the constitutive relation for near-critical xenon at large shear rates.

In the calculations we assumed that the force ratio C depends on $\dot{\gamma}\tau$ as well as x_0/δ and R/δ. We also assumed that the force at shear rate $\dot{\gamma}\tau$ divided by the force at small shear rate depends only on $\dot{\gamma}\tau$:

$$C_\gamma(\dot{\gamma}\tau) \equiv \frac{F(\text{shear thinning})}{F(\text{Newtonian})} = \frac{F(\dot{\gamma}\tau)}{F(0)} = C\left(\frac{R}{\delta}, \frac{x_0}{\delta}, \dot{\gamma}\tau\right) / C\left(\frac{R}{\delta}, \frac{x_0}{\delta}, 0\right). \tag{19}$$

Fig. 10 shows the magnitude and phase of the CFD calculations of $C_\gamma(\dot{\gamma}\tau)$.

There is no accurate analytical expression to compare with the CFD results. Therefore we derived an approximate expression [Eq. (B11) in Appendix B] and generalized it with free parameters. The resulting real functions

$$C_\gamma^{\text{magFit}}(\dot{\gamma}\tau) \equiv 1 - \alpha_{\text{mag}}\{1 - [1 + (\beta_{\text{mag}}/\alpha_{\text{mag}})\dot{\gamma}\tau]^{-p}\} \tag{20a}$$

and

$$C_\gamma^{\text{argFit}}(\dot{\gamma}\tau) \equiv 0 + \alpha_{\text{arg}}\{1 - [1 + (\beta_{\text{arg}}/\alpha_{\text{arg}})\dot{\gamma}\tau]^{-p}\} \tag{20b}$$

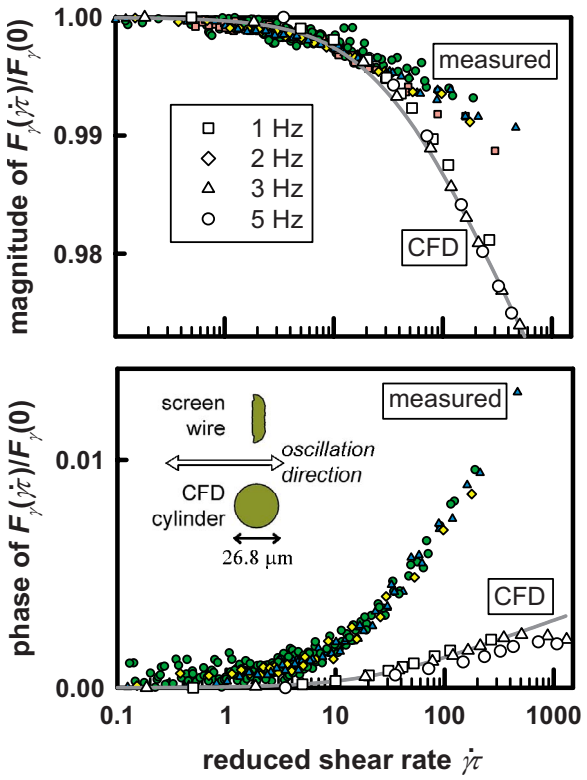

FIG. 10. (Color online) CFD and measured results for the magnitude and phase of the shear-thinning force ratio defined by Eq. (19). The data are normalized by the force expected in the absence of shear thinning, and the deviations from the values at $\dot\gamma\tau<1$ indicate shear thinning. (The data are from all of the runs and frequencies listed in Table II, with the exception of the measured 1-Hz phase data, which had unexpected noise.) The CFD calculations used a circular cross section that differed from that of the screen wire, and they assumed that viscoelasticity canceled out of the force ratio. The solid lines are fits of Eq. (20a) and (20b) to the 3-Hz CFD results at $\dot\gamma\tau<250$.

were fit to the magnitude and phase of the complex data, $C_\gamma(\dot\gamma\tau)$.

At small shear rates, the function $C_\gamma^{\mathrm{magFit}}$ reduces to

$$C_\gamma^{\mathrm{magFit}}(\dot\gamma\tau) \simeq 1 - p\beta_{\mathrm{mag}}\dot\gamma\tau, \tag{21}$$

and the magnitude of the force reduction becomes proportional to the fitted shear-rate scale factor β_{mag}. At large shear rates, the parameter α_{mag} allows for errors due to the approximate nature of Eq. (B11). The form of $C_\gamma^{\mathrm{argFit}}$ was chosen for simplicity to be similar to that of $C_\gamma^{\mathrm{magFit}}$.

Figure 10 shows that the magnitude of the CFD force ratio has little frequency dependence and is well described by the function $C_\gamma^{\mathrm{magFit}}$. In contrast, the phase results are frequency dependent and they deviate from $C_\gamma^{\mathrm{argFit}}$ at large shear rates. Table II gives the fitted values of α and β. The disagreement of the CFD results with the measured results at large shear rates likely occurred because Eq. (10) is not the constitutive relation for near-critical xenon at large shear rates. The fitting parameter α_{mag} allowed for such disagreement.

V. EXPERIMENTAL METHODS

A. Video calibration of the oscillator

Before the CVX-2 flight, we recorded video images of the oscillator's tip while driving the oscillator at 0.09 Hz, a frequency that was low enough to avoid the hydrodynamic nonlinearity due to the convective term of the Navier-Stokes equation. We calibrated the displacement of the tip by comparing its images to the known distance between adjacent screen wires. This calibration eliminated errors resulting from refraction by the xenon and the sapphire window. Another calibration, using an external test target, corrected a 2% aspect ratio error in the recorded images. Displacements

TABLE II. Coefficients for fits of Eq. (20a) and (20b) to the magnitude and phase of the force ratio C_γ. The CFD values were fit to the data shown in Fig. 10 in the range $\dot\gamma\tau<250$. The measured data were fit to the data shown in Figs. 1, 16, and 18. The measured values of α_{arg} and β_{arg} at 1 Hz are excluded from the averages.

CFD	f (Hz)	α_{mag}	β_{mag}	α_{arg}	β_{arg}
	1	0.452 ± 0.008	0.0100 ± 0.0002	0.050 ± 0.001	0.00156 ± 0.00003
	3	0.427 ± 0.009	0.0131 ± 0.0005	0.036 ± 0.001	0.00155 ± 0.00004
	5	0.454 ± 0.021	0.0119 ± 0.0010	0.026 ± 0.004	0.00115 ± 0.00020
	Average	0.444 ± 0.009	0.0117 ± 0.0009	0.037 ± 0.007	0.00142 ± 0.00013
Measured	f (Hz)	α_{mag}	β_{mag}	α_{arg}	β_{arg}
Run 2	5	0.097 ± 0.008	0.0172 ± 0.0017	0.145 ± 0.010	0.0125 ± 0.0008
Run 3	1	0.127 ± 0.004	0.0216 ± 0.0011	(0.099 ± 0.007)	(0.0677 ± 0.0092)
	3	0.096 ± 0.002	0.0238 ± 0.0010	0.175 ± 0.005	0.0104 ± 0.0004
	5	0.061 ± 0.005	0.0294 ± 0.0034	0.149 ± 0.011	0.0117 ± 0.0007
Run 4	2	0.104 ± 0.004	0.0245 ± 0.0014	0.141 ± 0.008	0.0114 ± 0.0008
	3	0.089 ± 0.004	0.0271 ± 0.0019	0.158 ± 0.006	0.0102 ± 0.0005
	Average	0.096 ± 0.087	0.0239 ± 0.0017	0.154 ± 0.006	0.0112 ± 0.0004

TABLE III. Outline of the 16 day temperature timeline.

Day	Operation	Purpose
0–1	Cool to T_c+1 K and then T_c+100 mK with lengthy pauses at both temperatures	Equilibrate the sample
2	Fast run through $T_c(-1\ \mu\mathrm{K/s})$ Drive oscillator with a low-amplitude frequency chirp spanning 0.06–25 Hz	Locate T_c to within 0.1 mK on the cell's thermometer
3	Warm to T_c+100 mK, pause, cool to T_c+3 mK	Equilibrate the sample
4–5	Slow run through $T_c(-0.025\ \mu\mathrm{K/s})$ Drive oscillator at large amplitudes at 5 Hz	Measure shear thinning at 5 Hz
6–14	Three more slow runs through T_c, each preceded by equilibration at T_c+100 mK	Measure shear thinning at other frequencies
15	Warm to T_c+5 K and pause for 12 h	Obtain calibration data far from T_c

measured over the full range of drive voltages yielded the derivative used in Eq. (13), $dx_{\mathrm{tip}}/dV_{\mathrm{out}}=(53.1\pm1.2)\ \mu\mathrm{m/V}$. The image resolution dominated the uncertainty of this result.

B. Temperature timeline

In orbit, the xenon sample did not have time to equilibrate fully at the smallest reduced temperatures because of critical slowing down. As in CVX, we programmed the temperature as a function of time [the "temperature timeline" $T(t)$] to ensure that temperature gradients remaining within the xenon caused negligibly small deviations of the local density from the critical density ρ_c. The timeline guaranteed that the local density of the xenon surrounding the oscillator remained within 0.15% of the xenon's average density. The viscometer was not affected by the larger "piston-effect" [42–46] density increases that formed close to the cell wall and far from the oscillator as the xenon was cooled from its boundaries.

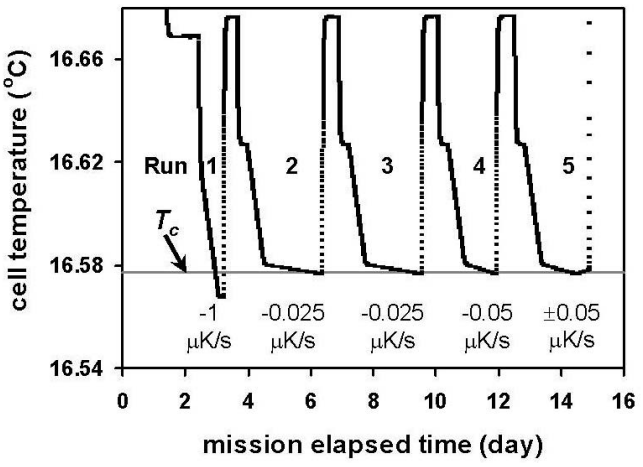

FIG. 11. The cell temperature during Space Shuttle mission STS-107. The first run, at the indicated ramp rate of $-1\ \mu\mathrm{K/s}$, located T_c to within 0.1 mK on the cell's thermometer. Later runs through $T_c=16.577$ °C used slower ramp rates. Each run was preceded by an equilibration at T_c+100 mK.

The timeline's two-part strategy was similar to that used during CVX. (See [3] for a longer discussion.) Far from T_c, the temperature was changed by large, rapid steps, which caused large, temporary inhomogeneities in the sample. Each step was followed by a waiting period that exceeded the xenon's equilibration time constant and permitted density inhomogeneities to decay. Close to T_c, the xenon's temperature was changed without waiting for equilibrium. However, the density remained within 0.3% of ρ_c, a tolerance sufficient for the viscosity measurements. The 16-day timeline used by CVX-2 is outlined in Table III and sketched in Fig. 11.

C. Oscillation sequences

During each of the slow runs through T_c the oscillator was periodically driven through a cycle of measurements that included one small drive amplitude and two or three large amplitudes. Table I lists the maximum shear rates associated with these amplitudes. Each run also included a few measurements at 0.5 Hz.

Each measurement comprised 32 s of data collection followed by 32 s during which the data were processed, stored, and transmitted to ground. The oscillator was driven at only one frequency at a time. If a chirp had been used (as in CVX), nonlinearity from hydrodynamics or shear thinning would have mixed frequencies. The time, temperature, and the functions $G(f)$ [Eq. (22)] and $\hat{V}_{\mathrm{in}}(f)$ were stored.

We conducted 2, 4, or 10 measurement cycles during each 90-min orbit. The measurements were synchronized with the orbit and averaged in pairs to reduce artifacts in the data synchronized with the space shuttle's orbit. During the 1997 CVX experiment, we observed such artifacts, which we attributed to the galactic cosmic-ray flux present at high latitudes [47] interacting with the capacitors used to detect the screen's position. No artifact was detected during the CVX-2 flight, perhaps because the orbital inclination of the 2003 mission was lower.

VI. REDUCTION OF THE EXPERIMENTAL DATA

The qualitative signature of shear thinning near T_c was a nonlinear dependence of the drag force F as a function of the

oscillator's amplitude x_0; the drag *decreased* as the amplitude increased. However, this signature was superimposed on an *increase* in the drag due to the convective term of the Navier-Stokes equation $[\rho(v\cdot\nabla)v]$, which is not related to critical fluctuations. Therefore, we measured just the convective contribution to F in the Newtonian fluid far from T_c and extrapolated its value into the non-Newtonian region near T_c. Dividing each non-Newtonian value of F by the extrapolated Newtonian value removed the Navier-Stokes nonlinearity and its noncritical dependence on x_0. Additional measurements made at a small amplitude x_{small} were used to remove the effect of viscoelasticity and its dependence on f. In this section we discuss the steps used to separate the effect of shear thinning from these other effects.

A. Data averaging

During the mission, the apparatus recorded 370 h of data, of which 85% were downlinked for real-time analysis. Fortunately, the hard disk drive was recovered from Columbia's debris in a condition that made 99% of the data available for analysis.

Within each measurement cycle, data taken at the same frequency and drive amplitude were averaged together. The recorded temperature was the average temperature during the acquisition of the small-amplitude data. The larger-amplitude data were taken later during the measurement cycle; their temperatures were interpolated between the temperatures of the two adjacent small-amplitude data sets.

B. Oscillator response

At small angular amplitudes θ_0, the oscillator response is [3]

$$G(f) \equiv \frac{\hat{\theta}(f)}{\hat{N}(f)} = \frac{1}{k}\left[1 - \left(\frac{f}{f_0}\right)^2 + i\left(\frac{\rho}{\rho_s}\right)\left(\frac{f}{f_0}\right)^2 B\left(\frac{R}{\delta}\right)\right]^{-1}. \tag{22}$$

Here k is the oscillator's torsion spring constant and f_0 is its resonance frequency in vacuum, both of which were corrected for electrostatic spring softening as described in Sec. III B. [For clarity, Eq. (22) does not show the frequency-dependent corrections that account for the gain and phase shifts due to anelasticity of the torsion spring and the electronic transfer function of the drive and detection circuits [3].] The oscillator's effective density is $\rho_s = \rho_l/\pi R^2$, where ρ_l is the wire's measured linear density. The definition of ρ_s assumes that the wire's cross section is circular, unlike an actual wire of the oscillator (see Fig. 7). However, the size and shape of the assumed cross section are unimportant because they shift only the magnitude of the function B. Choosing $R = 13.4$ μm made the values of $B(R/\delta)$ measured at small amplitude similar to those calculated for a circular cylinder of the same radius [3,5].

In Eq. (22), the dimensionless torque $B(R/\delta)$ that characterizes the entire oscillator is independent of θ_0, which allows it to be equated with the dimensionless force $B(R/\delta)$ that characterizes a single cylinder in Eq. (15). For large amplitudes, however, the oscillator torque is no longer proportional to θ_0, and the following generalization is required:

$$B\left(\frac{R}{\delta}\right) \Rightarrow B_{\text{osc}}\left(\frac{R}{\delta},\theta_0\right) \simeq \frac{3}{r_{\text{tip}}}\int_0^{r_{\text{tip}}} B\left(\frac{R}{\delta}\right) C\left(\frac{\theta_0 r}{\delta},\frac{R}{\delta}\right)\left(\frac{r}{r_{\text{tip}}}\right)^2 dr. \tag{23}$$

The oscillator response thus becomes a function of θ_0 as well as R/δ, and Eq. (22) generalizes to

$$G(f,\theta_0) \equiv \frac{\hat{\theta}(f)}{\hat{N}(f)} = \frac{1}{k}\left[1 - \left(\frac{f}{f_0}\right)^2 + i\left(\frac{\rho}{\rho_S}\right)\left(\frac{f}{f_0}\right)^2 B_{\text{osc}}\left(\frac{R}{\delta},\theta_0\right)\right]^{-1}. \tag{24}$$

Reference [5] gives more details.

C. Force on the tip wire

The torque on the oscillator comprised the torques of the screen's individual wires, each of which moved at a speed that was proportional to its distance from the torsion axis. For simplicity, we converted the measured response of the oscillator into the response of the wire located at the oscillator tip. Its displacement was

$$x_{\text{tip}}(t) = x_0\cos(\omega t) \cong \theta_0 r_{\text{tip}}\cos(\omega t). \tag{25}$$

The conversion allowed comparisons of the measurements with the CFD numerical calculations of the force on a single wire [5]. The conversion required the following four steps.

(i) *Obtain the dimensionless torque B_{osc} from the oscillator response G.* Equation (24) was solved to convert the measured response $G(f,\theta_0)$ into $B_{\text{osc}}(R/\delta,\theta_0)$, which describes the hydrodynamics of the entire oscillator. (Nonlinearity of the capacitive drive and detection required a correction that did not exceed 1.5% of $|G|$.) This step separated the hydrodynamic force from the effects of the nickel oscillator's inertia and torsion spring.

(ii) *Normalize the nonlinear response of the oscillator by its linear response.* The value of B_{osc} was normalized by its value at small amplitude to obtain the quantity

$$B'_{\text{osc}}\left(\frac{R}{\delta},\theta_0\right) \equiv \frac{B_{\text{osc}}(R/\delta,\theta_0)}{B(R/\delta)} \cong \frac{B_{\text{osc}}(R/\delta,\theta_0)}{B_{\text{osc}}(R/\delta,\theta_{\text{small}})}. \tag{26}$$

The linear response B of a single wire [Eq. (15)] is approximated here by the experimental value B_{osc} for the entire oscillator measured at the smallest amplitude θ_{small}. This approximation was accurate because θ_{small} always corresponded to $x_0/\delta < 0.1$. This step removed the temperature dependence of the Newtonian viscosity without relying on a detailed model of the oscillator. It also removed the effect of viscoelasticity (except for the part discussed below in Step 4).

(iii) *Obtain the nonlinear response C of the tip wire.* The response of the tip wire, normalized by its response at small amplitude, was obtained from the measured quantities θ_0, B'_{osc}, and the derivative of B'_{osc} with respect to θ_0 by use of the expression

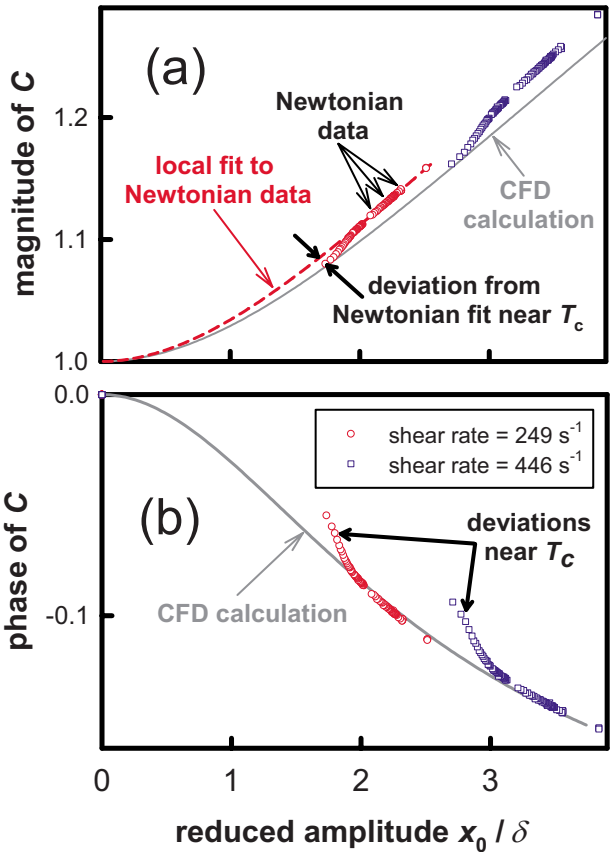

FIG. 12. (Color online) Magnitude and phase of the nonlinear response C at 3 Hz as a function of the reduced oscillation amplitude x_0/δ. The points are experimental data for two drive amplitudes. The solid lines are fits to CFD Newtonian data; their offsets from the experimental data in the Newtonian range (10 mK $< T - T_c <$ 100 mK) are due to the circular cross section of the CFD oscillator. (a) The dashed line is a fit to the 249 s^{-1} experimental data in the Newtonian range. The fit was extrapolated to $x_0/\delta = 0$ by using the same functional form that was fit to the CFD data. Deviations from the extrapolation are due to non-Newtonian behavior close to T_c. (b) Similar deviations were seen in the phase data.

$$C\left(\frac{R}{\delta}, \frac{x_0}{\delta}\right) = B'_{\mathrm{tip}}\left(\frac{R}{\delta}, \theta_0\right) = B'_{\mathrm{osc}}\left(\frac{R}{\delta}, \theta_0\right) + \frac{\theta_0}{3}\left[\frac{d}{d\theta_0} B'_{\mathrm{osc}}\left(\frac{R}{\delta}, \theta_0\right)\right]. \quad (27)$$

Equation (27) is derived in Ref. [5].

Figure 12 plots the nonlinear response C as a function of the reduced oscillation amplitude x_0/δ. Shear thinning close to the critical point caused C to deviate from the Newtonian behavior expected from both ground measurements and numerical calculations. The deviations were separated from the Newtonian behavior by fitting the Newtonian data, in the range from 10 to 100 mK above T_c, to the same functional form that described the CFD calculations.

(iv) *Separate the effect of shear thinning from the other nonlinearities.* Far from the critical point, the function C depends only on the dimensionless arguments x_0/δ and R/δ.

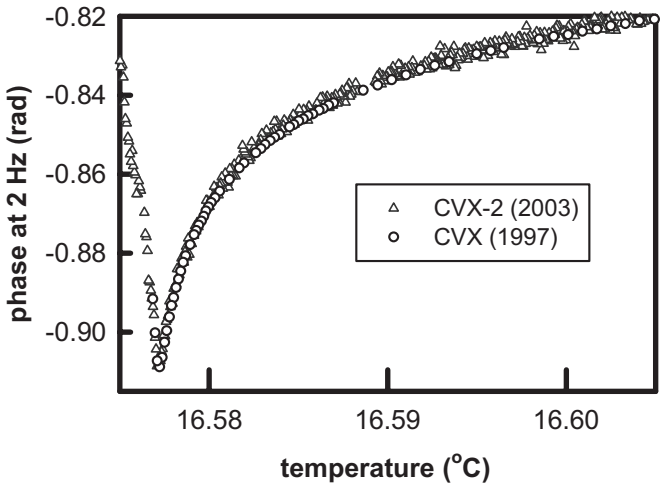

FIG. 13. Comparison of small-amplitude results from CVX and CVX-2. The CVX data for the phase of the hydrodynamic force on the oscillator at 2 Hz were adjusted vertically by 2.7 mrad and horizontally by 5.9 mK. The overlap of the data sets demonstrates the stability of the sample and oscillator.

Close to the critical point, C also depends on the reduced shear rate $\dot{\gamma}\tau$. As was done for the CFD analysis, we used Eq. (19), which assumes that the dependences of C on x_0/δ and $\dot{\gamma}\tau$ can be described as the product of $C(\dot{\gamma}\tau = 0)$ and a function $C_\gamma(\dot{\gamma}\tau)$ that depends only on the reduced shear rate $\dot{\gamma}\tau$. Far from T_c, shear thinning is negligible, and $C_\gamma(0) = 1$.

The denominator in Eq. (19), $C(R/\delta, x_0/\delta, 0)$, was obtained in three steps.

(1) C was measured at the same frequency but at temperatures far from T_c, so that $\omega\tau \ll 1$. There the viscosity was smaller and purely real.

(2) We estimated the value of C at the desired value of x_0/δ. The functional form that described the CFD calculations was fit to Newtonian data in the range 10 mK $< T - T_c <$ 100 mK and then extrapolated to values of x_0/δ for temperatures closer to T_c. The dashed line on Fig. 12 is an example of the extrapolation.

(3) We accounted for interaction of viscoelasticity with the oscillator's nonlinear hydrodynamic response by generalizing the viscous penetration length δ to a complex number δ^*. The value of C for complex x_0/δ^* was obtained as follows:

$$\frac{C\left(\frac{x_0}{\delta^*}, \frac{R}{\delta}, 0\right)}{C\left(\frac{x_0}{\delta}, \frac{R}{\delta}, 0\right)} \simeq 1 + \frac{1}{C}\frac{dC}{d\eta}[\eta(\omega) - \eta(0)] \simeq 1 + \frac{(x_0/\delta)}{2C}\frac{dC}{d(x_0/\delta)}\left(1 - \frac{\eta(\omega)}{\eta(0)}\right). \quad (28)$$

The complex viscoelasticity ratio $\eta(\omega)/\eta(0)$ was obtained from previous measurements [3], and the value and derivative of C were obtained from ground measurements [5]. (The derivative of C with respect to R/δ was neglected.) At $T_c + 0.1$ mK, corrections due to Eq. (28) were as large as 0.006 in relative magnitude and 0.006 rad in phase.

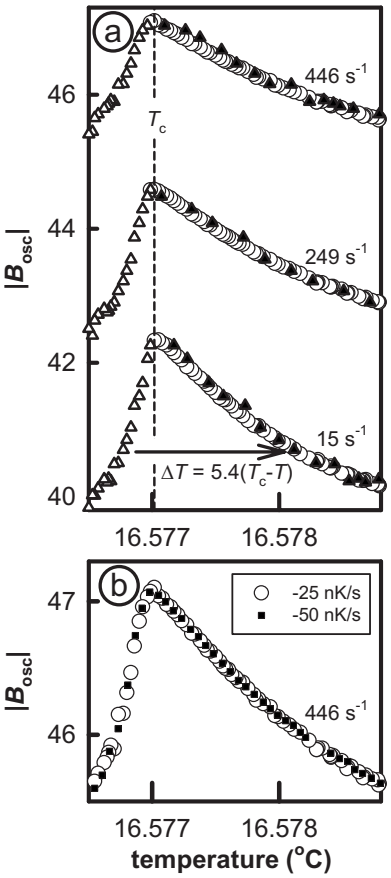

FIG. 14. (a) The magnitude of the reduced hydrodynamic force on the oscillator at 3 Hz for three shear rates. Translating the data below T_c by the amount ΔT (see text) causes them to lie on the data above T_c; the horizontal arrow indicates an example. The vertical dashed line indicates T_c determined by fitting Eq. (29) to the 15-s^{-1} data. (b) Superposed data from runs at different cooling rates. Similar agreement was seen at the smaller shear rates.

Appendix C lists averaged values of the magnitude and phase of C_γ.

VII. RESULTS

A. Sample and oscillator stability

Figure 13 demonstrates the stability of the sample and oscillator by comparing results from CVX-2 in 2003 with those from CVX in 1997. The results are in good agreement after adjusting the CVX data vertically by 2.7 mrad and horizontally by 5.9 mK. The phase shift is consistent with that seen in ground tests made in 2000, and the temperature adjustment accounts for a plausible thermistor drift during the intervening 5 years. This and similar comparisons of magnitude and phase at other frequencies indicated the absence of a significant change caused by, for example, mechanical shock or a xenon leak.

B. Determination of T_c

The critical temperature T_c was determined by fitting the following empirical function to the magnitude of the dimensionless torque $B_{\rm osc}$ in a narrow range of temperatures near T_c:

$$\frac{|B_{\rm osc}(\varepsilon)|}{|B_{\rm osc}(0)|} = 1 - a\varepsilon'^{c}(1 - e^{-d\varepsilon'}), \tag{29}$$

where $\varepsilon \equiv (T - T_c)/T_c$ and

$$\varepsilon' \equiv \begin{cases} \varepsilon + \Delta\varepsilon, & \varepsilon + \Delta\varepsilon > 0, \\ -b(\varepsilon + \Delta\varepsilon), & \varepsilon + \Delta\varepsilon < 0. \end{cases}$$

The parameter $\Delta\varepsilon$ accounted for the difference between the fitted T_c and a nominal initial value. The temperature scale factor b accounted for the asymmetry evident in Fig. 13; it was frequency dependent, perhaps because of viscoelasticity or shear thinning. When fitting Eq. (29), we reduced the frequency dependence by excluding data above a threshold (99% of the peak value). The fitted values of T_c were not sensitive to either the threshold or the fitted range of temperature.

During the flight, the fitted values of T_c changed by -13 μK/day, as determined from the smallest oscillation amplitudes. A linear function of time fit these values of T_c (runs 2–5) within 2 μK. This small time dependence was almost certainly due to thermometry drift because the post-flight measurement of the liquid-vapor meniscus had ruled out a significant sample leak.

The values of T_c determined from the largest oscillation amplitudes ($\dot{\gamma} \simeq 440$ s^{-1}) also changed by -13 μK/day; however, the fitted values were approximately 40 μK lower. Based on the discussion in Sec. II B, we neglected that temperature difference and assumed that T_c depended on time but not shear rate. We also note that the observed T_c shift of -40 μK was much smaller than the T_c shift predicted by Eq. (6), specifically $T_c(440\ \text{s}^{-1}) - T_c(0) = -350$ μK.

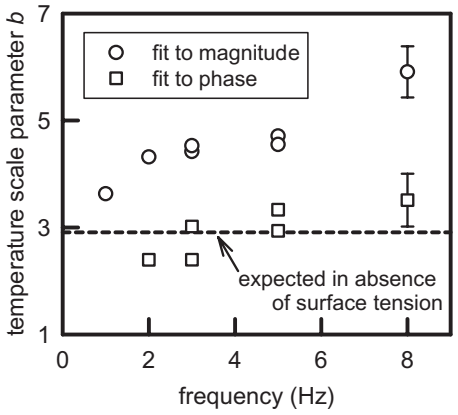

FIG. 15. Values of the temperature scale parameter b obtained from fits of Eq. (29) to the data at the lowest shear rates. Except for the 8-Hz data, the fit uncertainties are comparable to the point size.

C. Viscosity of phase-separating xenon

Remarkably, to within the temperature scale factor b, the data are symmetric about T_c. Figure 14(a) demonstrates that symmetry by translating the magnitude data below T_c by the amount $\Delta T = (1+b)(T_c - T) - a$. (We defined $a \equiv 0$ for the

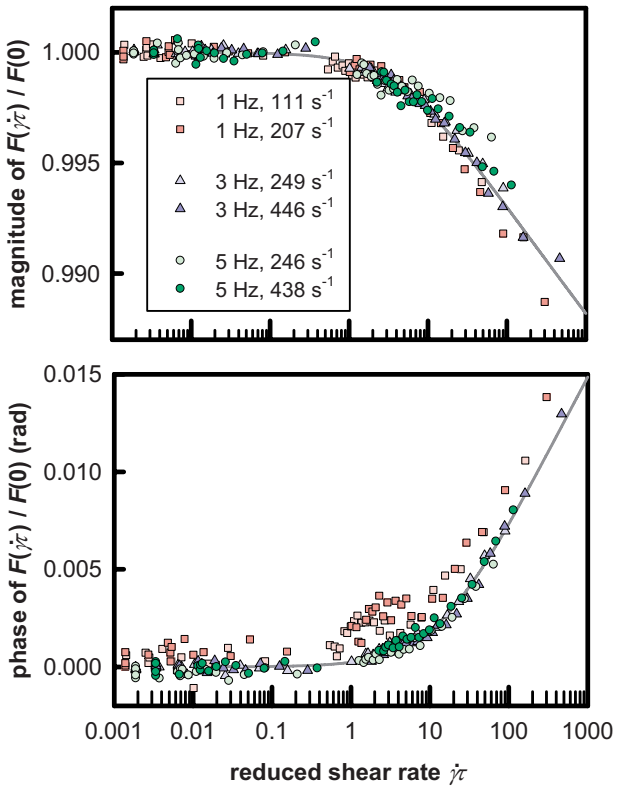

FIG. 16. (Color online) Magnitude and phase of the hydrodynamic force on the tip wire of the viscometer at several shear rates. The data (run 3) are normalized by the force expected in the absence of shear thinning. [See Eq. (19).] The reference curves were fit to the 3-Hz data in Fig. 1 (run 4).

lowest shear rate.) The translated data lie on the data above T_c for all three shear rates, which suggests that the rheology of the phase-separating xenon was similar to that of the single-phase xenon.

Figure 14(b) shows data from two runs with cooling rates that differed by a factor of 2. After adjusting for the thermometry drift, the data from these runs could be superimposed to temperatures as low as $T_c-0.5$ mK. Similar agreement occurred at the other two shear rates and in the phase as well as the magnitude. This history independence suggests that cooling below T_c created a liquid-vapor "emulsion" that behaved as a single fluid for as long as 5 h.

We estimated the value of b expected in the absence of surface tension by assuming that the viscosity depended only on the correlation length ξ. The dependence of ξ on the reduced temperature ε is $\xi_+\varepsilon^{-\nu}$ above T_c and $\xi_-|\varepsilon|^{-\nu}$ below T_c, where $\nu=0.63$ is the critical exponent and the amplitude ratio $\xi_+/\xi_-=1.96\pm0.01$ is well known from theory [48]. Equating the viscosities above and below T_c, specifically $\eta_+(\varepsilon)=\eta_-(-b\varepsilon)$, leads to

$$b=(\xi_+/\xi_-)^{1/\nu}=2.91\pm0.02. \tag{30}$$

This estimate of b is compared to the experimental values in Fig. 15. The values fitted to the magnitude of $B_{\rm osc}$ disagree with those fitted to the phase of $B_{\rm osc}$ as well as with the value estimated in the absence of surface tension. This disagreement suggests that surface tension affected the apparent viscosity below T_c. Further analysis is needed to compare the experimental data to Onuki's theory for viscosity enhancement by domains in the phase-separating fluid [49].

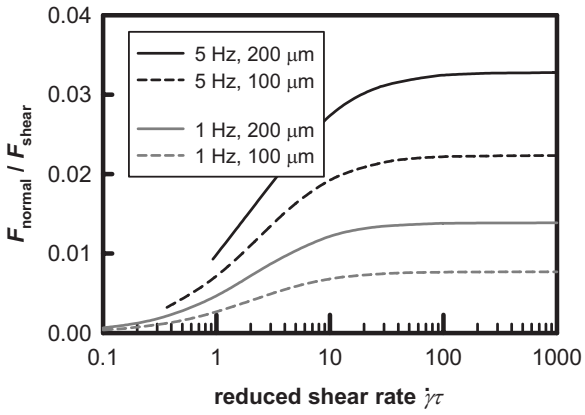

FIG. 17. Calculated effect of normal stress on a circular cylinder oscillating in a near-critical fluid. The oscillation amplitudes x_0 are representative of those used by CVX-2, for which the maximum values at 1 Hz and 5 Hz were, respectively, 430 μm and 130 μm. The calculated results show significant dependences on oscillation amplitude and frequency, but the measured data have no such dependences.

D. Qualitative evidence for shear thinning

Figure 16 plots data for the force ratio $C_\gamma(\dot\gamma\tau)$ measured at 1, 3, and 5 Hz (run 3). The 8-Hz data are not shown because they had a poor signal-to-noise ratio. (The 12-Hz data of run 5 were not plotted for the same reason.) As with the data of Fig. 1, the magnitude data scale with reduced shear rate even though the frequency varies by a factor of 5 and the shear rate varies by a factor of 4. The phase data demonstrate similar scaling, except that the 1-Hz data are displaced, perhaps due to a problem in subtracting the nonlinear background.

Figures 1, 10, 16, and 18 display qualitative evidence for near-critical shear thinning. The data for the force ratio C_γ scale better with reduced shear rate than with reduced temperature ε or reduced frequency $\omega\tau$, and they agree qualitatively with the CFD calculations of C_γ based on the Carreau-Yasuda relation. The CFD calculations predicted that shear thinning would cause the magnitude to decrease and the phase to increase. The measured results are described by the same empirical form, Eq. (20a) and (20b), used to describe the CFD results. However, as shown in Fig. 10, the quantitative disagreement is substantial. At $\dot\gamma\tau=1000$, for example, the calculated magnitude decrease is 3 times larger than the measured decrease.

It is unlikely that the quantitative disagreement with the CFD calculations resulted from either the wire's noncircular cross section or from an error in the data reduction. In the absence of shear thinning we found only small disagreements between the CFD values and the measured values of $C(R/\delta,x_0)$ [5]. Instead, we hypothesize that Eq. (10) is an inadequate constitutive relation for near-critical fluids. The

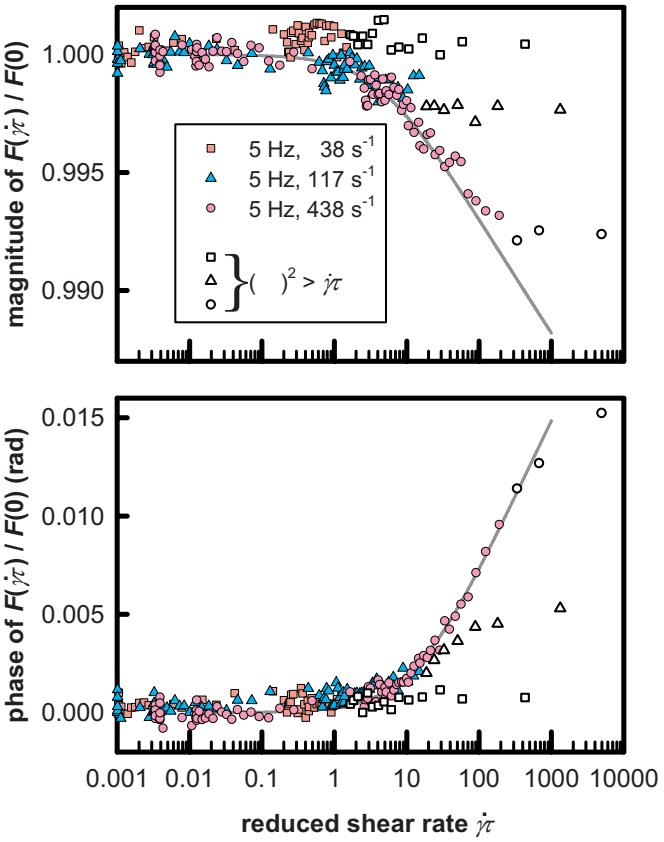

FIG. 18. (Color online) Magnitude and phase of the normalized hydrodynamic force [Eq. (19)] on the tip wire of the viscometer (run 2). The reference curves were fit to the 3-Hz data of Fig. 1. The open points, which deviate from the scaling with $\dot{\gamma}\tau$, are those for which $(\omega\tau)^2 > \dot{\gamma}\tau$.

lack of evidence for normal stress on the oscillator, discussed in Sec. VII E, also suggests the need for a better constitutive relation.

E. Lack of evidence of normal stress

We considered and rejected a correction to the data that would have accounted for normal stress on the oscillator. At small oscillation amplitudes, the size of such a correction would be negligible because the (radial) normal stress σ_{rr} is proportional to $(\dot{\gamma}\tau)^2$, while the shear stress is approximately proportional to $\dot{\gamma}\tau$. Also, the symmetry of the shear field would cause the contributions from the cylinder's leading and trailing edges to cancel. However, at large amplitudes the size of the expected correction is larger due to the asymmetry of the shear field. (See Fig. 9.) The shear rate is larger on the leading edge of the cylinder than on the trailing edge, and the unbalanced normal stresses could reduce the effect of shear thinning.

We estimated the size of the expected correction by combining Eq. (3) for the shear-thinned viscosity ratio $\eta(\dot{\gamma}_{r\theta})/\eta(0)$, Eq. (9) for the ratio $\sigma_{rr}/\sigma_{r\theta}$ of normal stress to shear stress (adapted to radial coordinates), and the numerically calculated distribution of shear rate $\dot{\gamma}_{r\theta}$ on the surface of a circular cylinder. Figure 17 plots the resulting force ratio

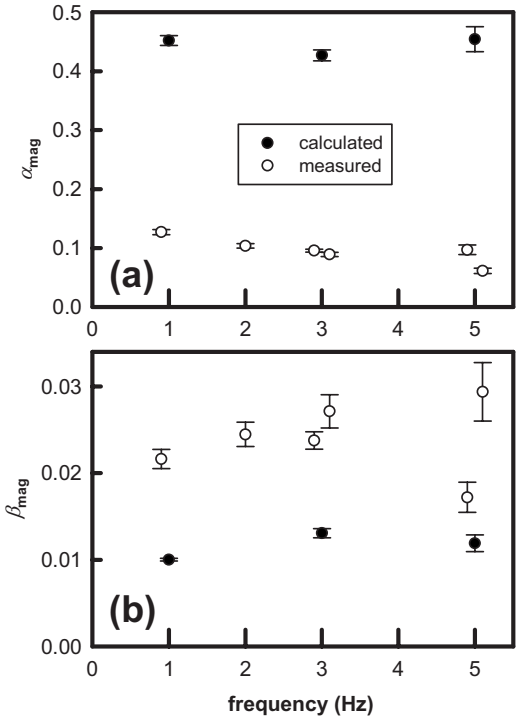

FIG. 19. Results of fitting Eq. (20a) and (20b) to the force ratio C_γ defined by Eq. (19). (Small horizontal displacements were added for clarity.) (a) The measured values of α_{mag} differ from the CFD values, which assume that the Carreau-Yasuda constitutive relation holds at all shear rates. (b) The values of the shear-rate scale factor β_{mag} fitted to the measurements have little frequency dependence and also disagree with the CFD values.

$$\frac{F_{\mathrm{normal}}}{F_{\mathrm{shear}}} = \frac{\int_0^{2\pi} \frac{\sigma_{rr}}{\sigma_{r\theta}} \dot{\gamma}_{r\theta} \cos(\theta) d\theta}{\int_0^{2\pi} \frac{\eta(\dot{\gamma})}{\eta(0)} \dot{\gamma}_{r\theta} \sin(\theta) d\theta}, \tag{31}$$

as a function of reduced shear rate for two representative frequencies and oscillation amplitudes. Here F_{normal} is the drag on the cylinder due to the asymmetric distribution of normal stress. Comparing Figs. 16 and 17 shows that the estimated drag is as much as 3 times that due to shear thinning and it depends on frequency and amplitude as well as reduced shear rate. In contrast, the measured data show no such dependences. Therefore, we rejected any correction for normal stress on the oscillator. Further theoretical work and more direct experimental measurements are needed to clarify the surprising absence of effects due to normal stress in xenon.

F. Constitutive relation at large reduced frequency

Figures 1 and 16 do not include data that violate the condition

$$(\omega\tau)^2 < \dot{\gamma}\tau \tag{32}$$

because those data do not scale with $\dot{\gamma}\tau$. This cutoff condition maximizes the number of data that scale with $\dot{\gamma}\tau$. The

TABLE IV. Relative contributions to the standard uncertainty of the measured value of the shear-rate scale factor A_γ

Component	Relative contribution	Comment
Fit of $(\beta_{mag})_{measured}$	0.07	0.0017/0.0239 (Table II)
Fit of $(\beta_{mag})_{CFD}$	0.08	0.0009/0.0117 (Table II)
Maximum shear rate $\dot{\gamma}$	0.10	Difference between experimental drag and CFD drag (Fig. 12)
Fluctuation relaxation time τ	0.15	$\tau_0=(1.15\pm0.17)$ ps [3]
Root sum of squares	0.21	

only justification for using Eq. (32) instead of the simpler cutoff $\omega\tau<1$ suggested by Eq. (11) is empirical. For the CVX-2 measurement conditions, Eq. (32) is approximately equivalent to $\omega\tau<x_0/R$; therefore, it is possible that the deviations at large $(\omega\tau)^2$ were caused by hydrodynamic phenomena instead of a failure of the constitutive relation.

Figure 18 shows the deviations associated with large reduced frequency by including all values of $C_\gamma(\dot{\gamma}\tau)$ (run 2). [For clarity, similar deviations that depended on frequency as well as oscillation amplitude were excluded by Eq. (32) from Figs. 1 and 16, which depict runs 4 and 3.] The deviations depend on oscillation amplitude as well as reduced shear rate, and they appear to saturate at a constant value that depends on the dimensionless ratio $\omega/\dot{\gamma}$; this agrees qualitatively with Das and Bhattacharjee's theoretical expression. However, Eq. (11) also predicts that increasing the frequency at fixed reduced shear rate will initially increase the shear thinning, but that behavior is not seen here. Instead, increasing the ratio $\omega/\dot{\gamma}$ only decreased the shear thinning.

G. Scale factor A_γ

As shown in Figs. 1, 16, and 18, the empirical functions of Eq. (20a) and (20b) provided adequate descriptions of the experimental data below the frequency cutoff. Table II lists the fitted values of α and β. Figure 19 plots the fitted values of α_{mag} and β_{mag} versus frequency. The measured values of α_{mag} are approximately 5 times smaller than the values fit to the CFD results (Table II). That difference likely occurred because the constitutive relation used in the CFD calculations does not accurately describe near-critical xenon at large shear rates.

The values of β_{arg} that were fit to the phase data (not shown but listed in Table II) also have little frequency dependence, but are approximately 8 times larger than the values fit to the CFD calculations. There are two likely reasons for this discrepancy. First, in contrast to C_γ^{magFit}, the form of the phase fitting function C_γ^{argFit} is not supported by the approximate calculation of Appendix B. Second, the phase is more sensitive to viscoelasticity errors of the assumed constitutive relation.

The parameter β_{mag} can be used to obtain a value for the shear-rate scale factor A_γ because it describes the oscillator's behavior at smaller shear rates where the approximate forms for the constitutive equation [Eq. (10)] and the oscillator response [Eq. (B12)] are likely to be accurate. Figure 19 shows that the fitted values of β_{mag} have little frequency dependence, but are larger than the values fit to the CFD results. Accounting for the ratio between the measured and CFD values of β_{mag} (Table II) yields the result

$$A_\gamma=\frac{(\beta_{mag})_{measured}}{(\beta_{mag})_{CFD}}(A_\gamma)_{CFD}=\frac{(0.0239)}{(0.0117)}(0.067)=0.137. \tag{33}$$

Table IV lists the relative contributions to the uncertainty of A_γ, of which the more important are due to the reduced shear rate. The total (standard) relative uncertainty is 21%, so that

$$A_\gamma=0.137\pm0.029. \tag{34}$$

This value, obtained at the liquid-vapor critical point of xenon, is approximately twice the value of 0.067 that was fit [14] to data obtained by Hamano *et al.* [13] at the consolute point of a micellar solution, but it is consistent with Oxtoby's mode-coupling result of 0.121.

VIII. FUTURE WORK

To date, the present experiment and its predecessor [3] comprise the only measurements of near-critical shear thinning and viscoelasticity in the same fluid. A significant improvement would be to measure both properties with a simpler flow field—say, Couette flow—so that interpretation of the oscillator's response at large shear rates could be straightforward. Using a near-critical binary mixture would avoid the difficulties caused by the large compressibility near the liquid-vapor critical point on Earth.

A challenge to theory is to explain the disagreement, shown in Fig. 10, between the CFD and experimental results at large shear rates. This will require an improved hydrodynamic model of the oscillator wire that includes a constitutive equation that is accurate at large shear rates. A CFD model seems necessary, although significant improvement of the analytical model in Appendix B may be possible. A second challenge would be to reconcile Das and Bhattacharjee's result for simultaneous shear thinning and viscoelasticity with Oxtoby's result and apply it to the present results.

ACKNOWLEDGMENTS

We thank the CVX-2 team at Glenn Research Center, especially Sue Motil, Jim Myers, and Don Priebe, for building and supporting the flight apparatus. We thank also the Hitchhiker team at NASA Goddard Space Flight Center, led by Tom Dixon and Katie Barthelme, for coordinating and operating FREESTAR. We thank Arnon Chait for his initial CFD calculations and for arranging Minwu Yao's collaboration. We acknowledge helpful conversations with Jack Douglas and Jan Sengers. We are grateful for the scientific opportunity given to us by the flight of STS-107 and the crew of the Space Shuttle Columbia. This work was funded, in part, by the NASA Fundamental Physics program under Contract No. C32966J.

APPENDIX A: CALCULATED SHEAR RATES

The force F per unit length on an oscillating cylinder is the integral of stresses due to the pressure p_R and the shear rate $\dot{\gamma}_{r\theta}$ at the oscillator's surface [50]. For a circular cylinder,

$$F = R\int_0^{2\pi} [p_R \cos(\theta) + \eta(\dot{\gamma})\dot{\gamma}_{r\theta}\sin(\theta)]d\theta, \qquad \text{(A1)}$$

where θ is the azimuthal angle around the cylinder. Shear thinning makes the viscosity $\eta(\dot{\gamma})$ depend on shear rate, but it also influences the flow field and thus p_R and $\dot{\gamma}_{r\theta}$.

We equated the shear rate of the experimental oscillator with a representation derived from CFD calculations that were valid at large oscillation amplitudes x_0. The oscillator was modeled as a circular cylinder oscillating in a Newtonian fluid. The force depends only weakly on the shape of the cross section when $\delta > R$ [5]. A Newtonian fluid was used because supplementary numerical calculations showed that shear thinning increased the shear rate by less than 1% at large x_0.

Appendix A 1 derives an analytical estimate of the shear rate at small oscillation amplitudes. Appendix A 2 summarizes the CFD calculations, which were normalized by the analytical estimate.

1. Analytical calculation of $\dot{\gamma}$ at small amplitudes

Stokes derived the force on a circular cylinder of radius R oscillating perpendicular to its axis at small amplitude. Stuart [50] summarized Stokes' derivation in modern nomenclature. The dimensionless force is

$$B_{\text{cyl}}\left(\frac{R}{\delta}\right) = i\left[1 + \frac{4K_1(kR)}{kRK_0(kR)}\right], \qquad \text{(A2)}$$

where $k \equiv (1+i)/\delta$, and K_n is the modified Bessel function of order n. Here we use the velocity field from Stokes' derivation to calculate the shear rate at the surface of the cylinder.

For a cylinder oscillating with velocity $v(t) = \text{Re}[v_0 e^{i\omega t}]$, the radial and azimuthal velocities in cylindrical coordinates are, respectively,

$$v_r = \frac{1}{r}\frac{\partial\psi}{\partial\theta} = \frac{1}{r}\left[\frac{A}{r} + BK_1(kr)\right]\cos(\theta)e^{i\omega t} \qquad \text{(A3)}$$

and

$$v_\theta = \frac{\partial\psi}{\partial r} = \frac{1}{r}\left[\frac{A}{r} + BK_1(kr) + BkrK_0(kr)\right]\sin(\theta)e^{i\omega t}, \qquad \text{(A4)}$$

where ψ is the stream function and $\theta = 0$ is defined by the direction of oscillation. The no-slip boundary condition on the cylinder determines the constants A and B:

$$A = R^2 v_0\left[1 + \frac{2}{kR}\frac{K_1(kR)}{K_0(kR)}\right], \quad B = -\frac{2v_0}{kK_0(kR)}. \qquad \text{(A5)}$$

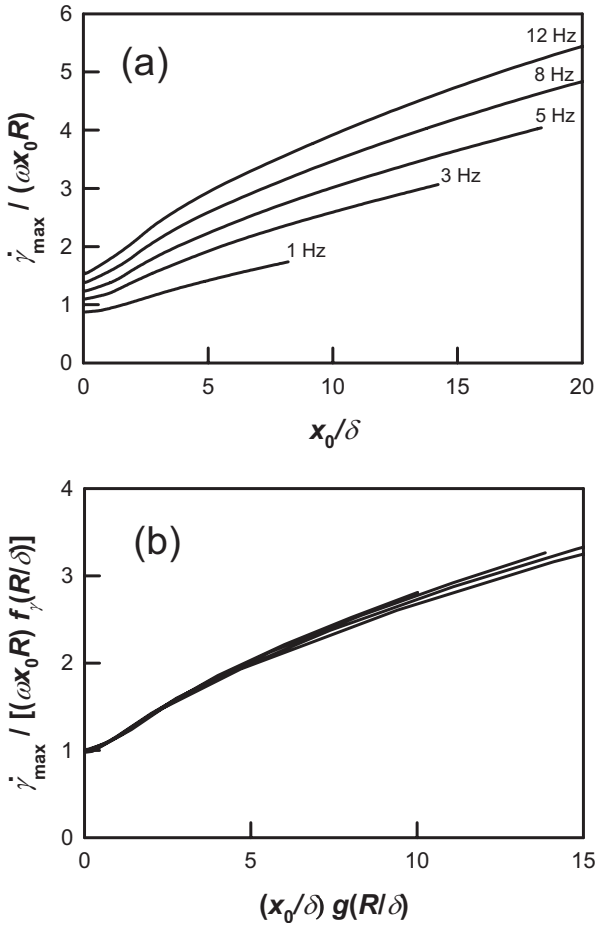

FIG. 20. Numerically calculated maximum shear rates at the surface of a transversely oscillating cylinder. (a) Shear rates normalized by $\omega x_0/R$ as a function of the reduced amplitude (x_0/δ). (b) Shear rates normalized by the analytical function $(\omega x_0/R) f_\gamma(R/\delta)$ as a function of the single variable $(x_0/\delta)g(R/\delta)$.

At $r = R$, the diagonal components of the rate-of-strain tensor disappear:

$$\{\dot{\gamma}_{rr}\}_{r=R} = 2\left\{\frac{\partial v_r}{\partial r}\right\}_{r=R} = 0,$$

$$\{\dot{\gamma}_{\theta\theta}\}_{r=R} = 2\left\{\frac{1}{r}\frac{\partial v_\theta}{\partial\theta} + \frac{v_r}{r}\right\}_{r=R} = 0. \qquad \text{(A6)}$$

The off-diagonal component is

$$\begin{aligned}\{\dot{\gamma}_{r\theta}\}_{r=R} &= \left\{r\frac{\partial}{\partial r}\left(\frac{v_\theta}{r}\right) + \frac{1}{r}\left(\frac{\partial v_r}{\partial\theta}\right)\right\}_{r=R} \\ &= -\left\{\left[\frac{4A}{r} + [4 + (kr)^2]BK_1(kr) + 2BkrK_0(kr)\right]\frac{\sin(\theta)e^{i\omega t}}{r^2}\right\}_{r=R} \\ &= 2\frac{v_0}{R}kR\frac{K_1(kR)}{K_0(kR)}\sin(\theta)e^{i\omega t}, \qquad \text{(A7)}\end{aligned}$$

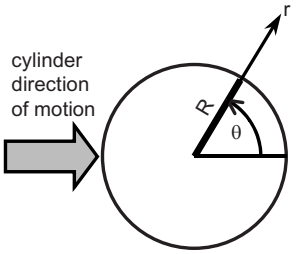

FIG. 21. Coordinates for the transversely oscillating cylinder.

which equals v_0/R times a function of R/δ. Defining the shear rate as the magnitude of the rate-of-strain tensor [18] gives

$$\dot{\gamma}(\theta,t) \equiv \left[\frac{1}{2}(\dot{\gamma}_{rr}^2 + \dot{\gamma}_{\theta\theta}^2 + \dot{\gamma}_{r\theta}^2 + \dot{\gamma}_{\theta r}^2)\right]_{r=R}^{1/2} = [\dot{\gamma}_{r\theta}^2]_{r=R}^{1/2}. \tag{A8}$$

Using $v_0 = i\omega x_0$ then gives

$$\dot{\gamma}_{\text{small}}(\theta,t) = \frac{\omega x_0}{R} f_\gamma\left(\frac{R}{\delta}\right)|\sin(\theta)||\sin(\omega t + \phi_\gamma)|, \tag{A9}$$

where

$$f_\gamma\left(\frac{R}{\delta}\right)\exp(i\phi_\gamma) \equiv 2kR\frac{K_1(kR)}{K_0(kR)}. \tag{A10}$$

The phase ϕ_γ depends on R/δ, but that dependence is weak in the range $0.06 < R/\delta < 0.38$ used by CVX-2. To a sufficient approximation,

$$f_\gamma(R/\delta) \cong a + b(R/\delta) + c(R/\delta)^2,$$

$$\phi_\gamma(R/\delta) \cong \phi_{\gamma 0}, \tag{A11}$$

where $a=0.525$, $b=3.387$, $c=-1.755$, and $\phi_{\gamma 0}=-0.40$ rad.

2. CFD calculation of $\dot{\gamma}$ at large amplitudes

CFD calculations for Newtonian xenon showed that large oscillation amplitudes increased the shear rate above the small-amplitude result of Eq. (A9). Figure 20 shows that increase by plotting normalized values of the maximum shear rate $\dot{\gamma}_{\max}$ as a function of reduced oscillation amplitude. We define $\dot{\gamma}_{\max} \equiv \dot{\gamma}(\theta_{\max}, \pi/2)$, where $\theta_{\max}$ is the location of the largest shear rate at time $\omega t = \pi/2$. (The largest shear rate, which occurs at time $\omega t = \pi/2 - \phi_\gamma$, is only a few percent larger.)

Large oscillation amplitudes also shifted $\theta_{\max}$ away from the value $\pi/2$ predicted by Eq. (A9). However, for the CVX-2 frequencies and amplitudes, the shift did not exceed 25° and the ratio $\dot{\gamma}(\theta_{\max}, \pi/2)/\dot{\gamma}(\pi/2, \pi/2)$ did not exceed 1.15.

In general, the ratio $\dot{\gamma}_{\max}/\dot{\gamma}_{\text{small}}$ is a function of the two variables x_0/δ and R/δ; however, we could describe the maximum shear rate by a function of the single variable $x_0 g(R/\delta)$ as follows:

$$\dot{\gamma}_{\max} \simeq \frac{\omega x_0}{R} f_\gamma\left(\frac{R}{\delta}\right) D\left[\frac{x_0}{\delta} g\left(\frac{R}{\delta}\right)\right]. \tag{A12}$$

The empirical functions in Eq. (A12) are

$$g(x) = \left[1 + \frac{0.08}{x}\right]^{-1}, \quad D(x) = 1 + \left[\frac{1.58}{x^{1/2}} + \frac{5.95}{x^2}\right]. \tag{A13}$$

For CVX-2, the reduced amplitude was $x_0/\delta < 4$; thus, Fig. 20(b) shows that Eq. (A12) is a good description of the maximum shear rate for CVX-2.

APPENDIX B: ANALYTICAL ESTIMATE OF THE REDUCTION OF FORCE ON AN OSCILLATING CIRCULAR CYLINDER DUE TO WEAK SHEAR THINNING

The weakness of shear thinning near the critical point allows useful approximations in the descriptions of the shear field and the dependence of viscosity on shear rate. The approximations allow an analytical estimate of the decrease of the force that opposes the transverse oscillations of a circular cylinder. We make the following three assumptions.

(i) Stokes' solution for small oscillations in a Newtonian fluid describes the shear field.

(ii) The Carreau-Yasuda relation, Eq. (3), describes the shear thinning.

(iii) There is no viscoelasticity.

For the cylinder shown in Fig. 21 and moving with velocity $v(t) = v_0 \cos(\omega t)$, the hydrodynamic force per unit length F exerted on the cylinder is [50]

$$\begin{aligned} F &= R\int_0^{2\pi} (p_{rr}\cos\theta - p_{r\theta}\sin\theta)d\theta \\ &= R\int_0^{2\pi} \left\{\left[2\eta\left(\frac{\partial v_r}{\partial r}\right)_R - p_R\right]\cos\theta \right. \\ &\quad \left. - \eta(\dot{\gamma})\left[r\frac{\partial}{\partial r}\left(\frac{\partial v_\theta}{\partial r}\right) + \frac{1}{r}\frac{\partial v_r}{\partial \theta}\right]\sin\theta\right\} d\theta \\ &= -R\int_0^{2\pi} \left\{p_R\cos\theta - \eta(\dot{\gamma}) r\frac{\partial}{\partial r}\left(\frac{\partial v_\theta}{\partial r}\right)\sin\theta\right\} d\theta. \end{aligned} \tag{B1}$$

Here p_R is the pressure and p_{rr} and $p_{r\theta}$ are the stresses at the cylinder surface, $r=R$. The radial shear rate there is $\partial v_r/\partial r = 0$, so the only effect of shear thinning is through the viscosity factor $\eta(\dot{\gamma})$ that multiplies the transverse shear rate $\partial v_\theta/\partial r$.

The first assumption allows the use of Eq. (A9) of Appendix A, so that

$$\dot{\gamma}(\theta,t) = \frac{v_0}{R} f_\gamma\left(\frac{R}{\delta}\right)\sin\theta\cos(\omega t + \phi_\gamma) \equiv \dot{\gamma}_0 \sin\theta\cos(\omega t'), \tag{B2}$$

where $\omega t' \equiv \omega t + \phi_\gamma$ and $\dot{\gamma}_0 \equiv (v_0/R) f_\gamma(R/\delta)$. The second assumption, when combined with the small value of the critical exponent for viscosity x_η, allows the shear thinning to be approximated as

$$\frac{\eta(0) - \eta(\dot{\gamma})}{\eta(0)} = \frac{\eta(0) - \eta(0)[1 + A_\gamma|\dot{\gamma}\tau|]^{-p}}{\eta(0)} \simeq p \ln[1 + A_\gamma|\dot{\gamma}\tau|], \tag{B3}$$

where $p \equiv x_\eta/(3+x_\eta) \approx 0.022$.

Substituting Eqs. (B2) and (B3) into Eq. (B1) expresses the force reduction ΔF as an integral around the perimeter of the cylinder:

$$\begin{aligned}
\Delta F &\equiv F(0) - F(\dot{\gamma}) \\
&= -R\eta(0)\int_0^{2\pi}\left(\frac{\eta(0) - \eta[\dot{\gamma}(\theta,t)]}{\eta(0)}\right)\dot{\gamma}(\theta,t)\sin\theta\, d\theta \\
&\cong -R\eta(0)\int_0^{2\pi} p \ln[1 + A_\gamma\dot{\gamma}_0\tau|\sin\theta||\cos(\omega t')|] \\
&\quad \times \dot{\gamma}_0 \sin\theta \sin\theta \cos(\omega t') d\theta \\
&= -R\eta(0)\int_0^{2\pi} p\dot{\gamma}_0(\sin\theta)^2[a_1(\theta)\cos(\omega t') \\
&\quad + a_3(\theta)\cos(3\omega t') + \cdots d\theta].
\end{aligned} \tag{B4}$$

The last line of Eq. (B4) decomposes the time dependence of ΔF into a Fourier sum that has only odd harmonics. The experimental quantity of most interest is the coefficient for the driving frequency,

$$a_1(\theta) = \frac{2}{\pi}\int_{-\pi/2}^{+\pi/2} \ln[1 + A|\cos x|](\cos x)^2 dx, \tag{B5}$$

where $x \equiv \omega t'$ and $A \equiv A_\gamma\dot{\gamma}_0\tau|\sin\theta| \leq 20$. Evaluating a_1 in the limits of large and small reduced shear rate yields

$$a_1(\theta) = \begin{cases} \ln\left(\dfrac{e^{1/2}}{2}A\right), & A\cos x \gg 1, \\ \dfrac{8}{3\pi}A, & A\cos x \ll 1. \end{cases} \tag{B6}$$

The following simple approximation is accurate to within $\pm 3\%$ for all values of $A\cos(x)$:

$$a_1(\theta) \cong \ln\left(1 + \frac{e^{1/2}}{2}A\right). \tag{B7}$$

Substituting Eq. (B7) into Eq. (B4) yields the force reduction at the driving frequency:

$$\Delta F = -p\dot{\gamma}_0\cos(\omega t')R\eta(0)\int_0^{2\pi}\ln\left(1 + \frac{e^{1/2}}{2}A\right)(\sin\theta)^2 d\theta. \tag{B8}$$

Rewriting the integral in terms of $\cos\theta$ gives Eq. (B8) the same form as Eq. (B5). Solving it with the same approximation yields

$$\begin{aligned}
\Delta F &\cong -\pi R p\dot{\gamma}_0\cos(\omega t')\eta(0)\ln\left(1 + \frac{e}{4}A_\gamma\dot{\gamma}_0\tau\right) \\
&\cong -\pi R\dot{\gamma}_0\Delta\eta[(e/4)\dot{\gamma}_0]\cos(\omega t'),
\end{aligned} \tag{B9}$$

where $\Delta\eta(x) \equiv \eta(x) - \eta(0)$.

Now we compare the force reduction ΔF to the force F in the absence of shear thinning. Stokes' solution in modern nomenclature is [50]

$$\begin{aligned}
F &= -i\pi\rho\omega R^2 v_0 e^{i\omega t}\left[1 + \frac{4K_1(kR)}{kRK_0(kR)}\right] \\
&= -\pi R\eta e^{i\omega t}\left[\frac{v_0}{R}(kR)^2 + 2(\dot{\gamma}_0 e^{i\phi_\gamma})\right] \\
&\simeq -2\pi R\eta\dot{\gamma}_0 e^{i\phi_\gamma}e^{i\omega t},
\end{aligned} \tag{B10}$$

where $k \equiv (1+i)/\delta$ and K_n is the modified Bessel function of order n.

The first term of Eq. (B10) represents periodic acceleration of the fluid displaced by the wire, and the second term represents viscous drag and inertia. For the conditions of the CVX-2 experiment, we ignored the second term because its magnitude is more than 20 times smaller than the magnitude of the second term. Expressing Eq. (B9) in complex notation and dividing it by Eq. (B10) gives the relative reduction of the force due to shear thinning:

$$\frac{\Delta F}{F} \simeq \frac{-\pi R\Delta\eta[(e/4)\dot{\gamma}_0]e^{i\phi_\gamma}e^{i\omega t}}{-2\pi R\eta(0)\dot{\gamma}_0 e^{i\phi_\gamma}e^{i\omega t}} = \frac{1}{2}\frac{\Delta\eta[(e/4)\dot{\gamma}_0]}{\eta(0)}. \tag{B11}$$

The function fit to the magnitude data, Eq. (20a) and (20b), was obtained from Eq. (B11) by replacing the factors 1/2

TABLE V. Standard uncertainties of the data tables.

Quantity	Uncertainty	Method
$T - T_c$	2 μK	Time dependence of T_c (Sec. VII B)
Maximum shear rate	10%	Difference between experimental drag and CFD drag (Fig. 12)
Fluctuation relaxation time	15%	$\tau_0 = (1.15 \pm 0.17)$ ps [3]
mag(C_γ)	0.002	Difference due to alternate extrapolation
arg(C_γ)	0.002 rad	Difference due to alternate extrapolation

TABLE VI. Run 2 (5 Hz).

$f=5$ Hz			$\dot{\gamma}\tau=\dot{\gamma}_1\tau$		$\dot{\gamma}\tau=3.08\dot{\gamma}_1\tau$		$\dot{\gamma}\tau=11.07\dot{\gamma}_1\tau$	
$T-T_c$ (mK)	$\omega\tau$	$\dot{\gamma}_1\tau$	mag(C_γ)	arg(C_γ) (mrad)	mag(C_γ)	arg(C_γ) (mrad)	mag(C_γ)	arg(C_γ) (mrad)
99.270	2.9×10^{-4}	4.5×10^{-4}	1.0000	0.4	1.0002	0.4	1.0003	0.0
91.794	3.4×10^{-4}	5.3×10^{-4}	0.9996	0.4	0.9998	0.5	0.9997	0.1
61.304	8.7×10^{-4}	1.3×10^{-3}	0.9998	0.0	0.9999	0.0	1.0000	−0.4
49.482	1.2×10^{-3}	1.8×10^{-3}	1.0001	0.4	1.0001	0.4	1.0001	0.0
42.594	1.6×10^{-3}	2.4×10^{-3}	0.9999	0.1	0.9998	0.2	0.9998	−0.2
29.946	3.3×10^{-3}	4.9×10^{-3}	1.0005	0.4	1.0003	0.4	1.0003	0.0
17.265	1.1×10^{-2}	1.6×10^{-2}	1.0003	0.3	0.9999	0.3	0.9999	−0.1
5.347	1.8×10^{-1}	2.5×10^{-1}	1.0007	0.6	0.9997	0.8	0.9994	0.6
2.751	3.7×10^{-1}	5.0×10^{-1}	1.0004	0.7	0.9991	0.9	0.9983	1.1
2.379	5.0×10^{-1}	6.6×10^{-1}	1.0008	0.5	0.9994	0.8	0.9986	1.0
2.078	6.5×10^{-1}	8.6×10^{-1}	1.0007	0.2	0.9994	0.8	0.9984	1.1
1.881	7.9×10^{-1}	1.0×10^{0}	1.0010	0.5	0.9997	0.9	0.9987	1.4
1.726	9.4×10^{-1}	1.2×10^{0}	1.0013	0.5	0.9997	0.9	0.9985	1.5
1.590	1.1×10^{0}	1.4×10^{0}	1.0009	0.5	0.9994	1.0	0.9981	1.8
1.465	1.3×10^{0}	1.7×10^{0}	1.0012	0.4	0.9995	1.1	0.9980	1.9
1.355	1.5×10^{0}	2.0×10^{0}	1.0010	0.2	0.9991	1.0	0.9974	2.1
1.211	1.9×10^{0}	2.5×10^{0}	1.0004	0.8	0.9987	1.7	0.9969	2.9
1.105	2.3×10^{0}	2.9×10^{0}	1.0002	0.6	0.9981	1.5	0.9960	3.1
0.980	2.9×10^{0}	3.7×10^{0}	1.0008	0.5	0.9989	1.5	0.9966	3.4
0.852	3.8×10^{0}	4.9×10^{0}	1.0006	0.4	0.9985	1.6	0.9957	3.9
0.723	5.3×10^{0}	6.8×10^{0}	1.0007	0.7	0.9983	2.0	0.9952	5.0
0.601	7.7×10^{0}	9.8×10^{0}	1.0015	0.5	0.9991	2.1	0.9953	5.9
0.477	1.2×10^{1}	1.5×10^{1}	1.0003	0.5	0.9978	2.5	0.9936	7.2
0.341	2.5×10^{1}	3.1×10^{1}	1.0005	0.7	0.9977	3.6	0.9927	9.7
0.193	8.4×10^{1}	1.0×10^{2}	1.0003	1.0	0.9974	4.6	0.9915	12.9

and $A_\gamma(e/4)$ with the free parameters $\alpha_{\rm mag}$ and $\beta_{\rm mag}/\alpha_{\rm mag}$ as follows:

$$\frac{F-\Delta F}{F} = 1-\frac{1}{2}\frac{\Delta\eta[(e/4)\dot{\gamma}_0]}{\eta(0)}$$
$$= 1-\frac{1}{2}\{1-[1+A_\gamma(e/4)|\dot{\gamma}_0\tau|]^{-p}\}$$
$$\to 1-\alpha_{\rm mag}\{1-[1+(\beta_{\rm mag}/\alpha_{\rm mag})|\dot{\gamma}_0\tau|]^{-p}\}. \quad \text{(B12)}$$

APPENDIX C: DATA TABLES

Table V gives the uncertainties of the data. The most important uncertainty was introduced by the function used to extrapolate the denominator of Eq. (19) from the Newtonian range to the shear-thinning range [step (iv) of Sec. VI C]. The function had the same form as the one that described the CFD Newtonian calculations. To estimate the uncertainty due to the function's form, we replaced it with a simpler, linear function of x_0/δ and calculated the change of the extrapolation.

With the exception of the 1-Hz phase data, the statistical uncertainties are much smaller [0.02% for mag(C_γ) and 0.0002 rad for arg(C_γ)].

Tables VI–VIII list the magnitude and phase of the reduced force C_γ [Eq. (28)] as functions of the reduced shear rate $\dot{\gamma}\tau$. The tables were created by averaging the data displayed in the figures in groups of N points. For $T-T_c<2$ mK, either $N=2$ (runs 2 and 3) or $N=1$ (run 4). Further from T_c, $N=5$ for all runs. The 8-Hz data of run 3 and the 12-Hz data of run 5 are not listed due to their poor signal-to-noise ratio.

Each run used several drive amplitudes to achieve different shear rates (see columns 4–7 of Table I). In Tables VI–VIII, the reduced shear rate associated with smallest drive amplitude is in the column labeled $\dot{\gamma}_1\tau$ and the reduced shear rates for the larger amplitudes are expressed as multiples of $\dot{\gamma}_1\tau$. For example, for the first line of Table VI the reduced shear rate for columns 6 and 7 is $(3.08)(4.5\times10^{-4})=1.4\times10^{-3}$.

TABLE VII. Run 3 (1, 3, 5 Hz).

$f=1$ Hz			$\dot{\gamma}\tau=\dot{\gamma}_1\tau$		$\dot{\gamma}\tau=1.89\dot{\gamma}_1\tau$	
$T-T_c$ (mK)	$\omega\tau$	$\dot{\gamma}_1\tau$	mag(C_γ)	arg(C_γ) (mrad)	mag(C_γ)	arg(C_γ) (mrad)
94.089	7.0×10^{-5}	1.4×10^{-3}	1.0000	0.2	1.0000	0.3
49.223	2.4×10^{-4}	4.7×10^{-3}	1.0001	0.4	1.0001	0.6
30.214	7.5×10^{-4}	1.5×10^{-2}	1.0000	0.2	1.0000	0.7
6.577	4.1×10^{-2}	7.7×10^{-1}	0.9997	0.8	0.9996	1.5
2.419	9.7×10^{-2}	1.8×10^{0}	0.9993	1.8	0.9992	2.6
2.001	1.4×10^{-1}	2.6×10^{0}	0.9992	2.5	0.9990	3.2
1.768	1.8×10^{-1}	3.4×10^{0}	0.9990	2.4	0.9988	2.9
1.539	2.4×10^{-1}	4.4×10^{0}	0.9991	2.1	0.9987	3.4
1.311	3.3×10^{-1}	6.1×10^{0}	0.9987	2.1	0.9982	3.2
0.998	5.7×10^{-1}	1.1×10^{1}	0.9984	2.1	0.9977	3.3
0.716	1.1×10^{0}	2.1×10^{1}	0.9973	3.5	0.9962	4.7
0.488	2.5×10^{0}	4.5×10^{1}	0.9959	5.2	0.9941	7.2
0.238	1.4×10^{1}	2.5×10^{2}	0.9926	9.4	0.9896	12.4
$f=3$ Hz			$\dot{\gamma}\tau=\dot{\gamma}_1\tau$		$\dot{\gamma}\tau=1.79\dot{\gamma}_1\tau$	
93.979	2.1×10^{-4}	3.7×10^{-3}	1.0001	−0.1	1.0001	0.0
49.191	7.1×10^{-4}	1.2×10^{-2}	1.0000	−0.1	0.9999	0.0
30.151	2.3×10^{-3}	3.8×10^{-2}	1.0001	−0.1	1.0001	0.0
6.934	1.1×10^{-1}	1.7×10^{0}	0.9996	0.3	0.9995	0.4
2.451	2.8×10^{-1}	4.2×10^{0}	0.9990	0.8	0.9987	1.1
2.031	4.1×10^{-1}	6.0×10^{0}	0.9985	1.2	0.9982	1.5
1.794	5.2×10^{-1}	7.6×10^{0}	0.9983	1.2	0.9979	1.5
1.569	6.8×10^{-1}	9.9×10^{0}	0.9983	1.3	0.9976	1.8
1.333	9.4×10^{-1}	1.4×10^{1}	0.9980	1.7	0.9971	2.3
1.040	1.6×10^{0}	2.2×10^{1}	0.9975	2.1	0.9964	2.9
0.745	3.1×10^{0}	4.3×10^{1}	0.9966	3.4	0.9951	4.5
0.514	6.6×10^{0}	9.1×10^{1}	0.9950	5.6	0.9929	7.3
0.269	3.0×10^{1}	4.1×10^{2}	0.9931	9.4	0.9903	11.9
$f=5$ Hz			$\dot{\gamma}\tau=\dot{\gamma}_1\tau$		$\dot{\gamma}\tau=1.79\dot{\gamma}_1\tau$	
93.870	3.5×10^{-4}	3.6×10^{-3}	1.0001	−0.3	1.0001	−0.1
48.788	1.2×10^{-3}	1.2×10^{-2}	0.9999	−0.3	1.0000	0.0
28.822	4.2×10^{-3}	4.1×10^{-2}	0.9999	−0.3	0.9998	0.0
6.205	2.0×10^{-1}	1.8×10^{0}	0.9997	0.1	0.9995	0.6
2.414	4.9×10^{-1}	4.2×10^{0}	0.9987	0.6	0.9983	1.4
1.969	7.2×10^{-1}	6.2×10^{0}	0.9985	0.9	0.9980	1.7
1.735	9.3×10^{-1}	8.0×10^{0}	0.9986	1.1	0.9979	2.0
1.504	1.2×10^{0}	1.1×10^{1}	0.9984	1.1	0.9976	2.1
1.278	1.7×10^{0}	1.5×10^{1}	0.9986	1.5	0.9977	2.7
0.953	3.1×10^{0}	2.6×10^{1}	0.9980	2.2	0.9968	3.8
0.682	6.2×10^{0}	5.1×10^{1}	0.9971	3.4	0.9954	5.4
0.458	1.4×10^{1}	1.1×10^{2}	0.9962	5.1	0.9939	8.0
0.203	1.1×10^{2}	8.5×10^{2}	0.9952	8.4	0.9924	12.5

TABLE VIII. Run 4 (2, 3 Hz).

$f=2$ Hz			$\dot{\gamma}\tau=\dot{\gamma}_1\tau$		$\dot{\gamma}\tau=1.83\dot{\gamma}_1\tau$	
$T-T_c$ (mK)	$\omega\tau$	$\dot{\gamma}_1\tau$	mag(C_γ)	arg(C_γ) (mrad)	mag(C_γ)	arg(C_γ) (mrad)
80.929	2.3×10^{-4}	4.8×10^{-3}	1.0000	0.1	1.0001	0.0
45.637	5.7×10^{-4}	1.2×10^{-2}	0.9999	0.0	1.0000	−0.1
22.648	3.2×10^{-3}	6.5×10^{-2}	1.0000	0.1	1.0000	0.1
3.505	1.4×10^{-1}	2.7×10^{0}	0.9992	0.8	0.9990	0.7
1.926	3.0×10^{-1}	5.7×10^{0}	0.9987	1.0	0.9983	1.1
1.677	4.0×10^{-1}	7.4×10^{0}	0.9984	1.2	0.9978	1.4
1.391	5.9×10^{-1}	1.1×10^{1}	0.9982	1.5	0.9976	1.5
1.064	9.9×10^{-1}	1.8×10^{1}	0.9975	2.3	0.9966	2.5
0.823	1.7×10^{0}	3.0×10^{1}	0.9966	3.0	0.9953	3.6
0.570	3.6×10^{0}	6.4×10^{1}	0.9953	4.5	0.9934	5.5
0.318	1.3×10^{1}	2.2×10^{2}	0.9932	7.6	0.9904	9.5
$f=3$ Hz			$\dot{\gamma}\tau=\dot{\gamma}_1\tau$		$\dot{\gamma}\tau=1.79\dot{\gamma}_1\tau$	
80.681	3.4×10^{-4}	5.9×10^{-3}	0.9999	−0.2	1.0000	−0.1
45.565	8.6×10^{-4}	1.4×10^{-2}	1.0000	−0.2	1.0000	−0.1
22.521	4.9×10^{-3}	7.9×10^{-2}	0.9999	−0.2	0.9999	−0.1
3.479	2.1×10^{-1}	3.2×10^{0}	0.9990	0.6	0.9988	0.7
1.921	4.6×10^{-1}	6.7×10^{0}	0.9985	1.1	0.9981	1.4
1.671	6.0×10^{-1}	8.8×10^{0}	0.9983	1.2	0.9977	1.6
1.386	8.9×10^{-1}	1.3×10^{1}	0.9983	1.5	0.9976	1.9
1.058	1.5×10^{0}	2.1×10^{1}	0.9973	2.3	0.9963	2.9
0.816	2.6×10^{0}	3.6×10^{1}	0.9965	3.1	0.9951	4.1
0.563	5.5×10^{0}	7.6×10^{1}	0.9952	4.7	0.9932	6.2
0.312	2.0×10^{1}	2.7×10^{2}	0.9935	8.1	0.9908	10.4

[1] J. V. Sengers, Int. J. Thermophys. **6**, 203 (1985).
[2] P. C. Hohenberg and B. I. Halperin, Rev. Mod. Phys. **49**, 435 (1977).
[3] R. F. Berg, M. R. Moldover, and G. A. Zimmerli, Phys. Rev. E **60**, 4079 (1999).
[4] H. Hao, R. A. Ferrell, and J. K. Bhattacharjee, Phys. Rev. E **71**, 021201 (2005).
[5] Ground-based hydrodynamic studies by R. F. Berg, M. Yao, G. A. Zimmerli, and C. H. Panzarella. See NASA/CR-2007-215050 (2007).
[6] J. C. Allegra, A. Stein, and G. F. Allen, J. Chem. Phys. **55**, 1716 (1971).
[7] A. Stein, J. C. Allegra, and G. F. Allen, J. Chem. Phys. **55**, 4265 (1971).
[8] F. R. Meeks and C. C. Yang, J. Phys. Chem. **75**, 2619 (1971).
[9] V. C. Tsai and D. McIntyre, J. Chem. Phys. **60**, 937 (1974).
[10] K. Hamano, T. Nomura, T. Kawazura, and N. Kuwahara, Phys. Rev. A **26**, 1153 (1982).
[11] I. L. Pegg and I. A. McLure, Mol. Phys. **53**, 897 (1984).
[12] I. A. McLure and P. J. Clements, Ber. Bunsenges. Phys. Chem **101**, 114 (1997).
[13] K. Hamano, J. V. Sengers, and A. H. Krall, Int. J. Thermophys. **16**, 355 (1995).
[14] R. F. Berg, J. Rheol. **48**, 1365 (2004).
[15] D. W. Oxtoby, J. Chem. Phys. **62**, 1463 (1975).
[16] K. Hamano, N. Kuwahara, I. Mitsushima, K. Kubota, and T. Kamura, J. Chem. Phys. **94**, 2172 (1991).
[17] S. Bair, C. McCabe, and P. T. Cummings, Phys. Rev. Lett. **88**, 058302 (2002).
[18] R. B. Bird, R. C. Armstrong, and O. Hassager, *Dynamics of Polymeric Liquids* (Wiley, New York, 1987), Vol. 1.
[19] A. Onuki, Phys. Lett. **64A**, 115 (1977).
[20] P. Das and J. K. Bhattacharjee, Phys. Rev. E **71**, 036145 (2005).
[21] J. C. Nieuwoudt and J. V. Sengers, Physica A **147**, 368 (1987).
[22] A. Onuki, J. Phys.: Condens. Matter **9**, 6119 (1997).

[23] A. Onuki, *Phase Transition Dynamics* (Cambridge University Press, Cambridge, England, 2002).
[24] R. Folk and G. Moser, Int. J. Thermophys. **19**, 1003 (1998).
[25] J. K. Bhattacharjee and R. A. Ferrell, Phys. Rev. A **27**, 1544 (1983).
[26] A. Onuki and K. Kawasaki, Phys. Lett. **75A**, 485 (1980).
[27] C. M. Sorensen, B. J. Ackerson, R. C. Mockler, and W. J. O'Sullivan, Phys. Rev. A **13**, 1593 (1976).
[28] D. W. Oxtoby and H. Metiu, Phys. Rev. Lett. **36**, 1092 (1976).
[29] D. W. Oxtoby, Phys. Rev. A **15**, 1251 (1977).
[30] E. Ducros, S. Haouache, J. Rouch, K. Hamano, K. Fukuhara, and P. Tartaglia, Phys. Rev. E **50**, 1291 (1994).
[31] P. Das and J.K. Bhattacharjee, Phys. Rev. E **63**, 020202(R) (2001).
[32] J. F. Douglas, Macromolecules **25**, 1468 (1992).
[33] P. J. Carreau, Ph.D. thesis, University of Wisconsin, 1968.
[34] K. Yasuda, Ph.D. thesis, Massachusetts Institute of Technology, 1979.
[35] K. Yasuda, R. C. Armstrong, and R. E. Cohen, Rheol. Acta **20**, 163 (1981).
[36] A. Onuki and K. Kawasaki, Ann. Phys. (N.Y.) **121**, 456 (1979).
[37] J. V. Sengers (private communication).
[38] J. F. Douglas (private communication).
[39] J. M. Dealy and K. F. Wissbrun, *Melt Rheology and its Role in Plastics Processing* (Van Nostrand, New York, 1990).
[40] W. P. Cox and E. H. Merz, J. Polym. Sci. **28**, 619 (1958).
[41] R. F. Berg, G. A. Zimmerli, and M. R. Moldover, Int. J. Thermophys. **19**, 481 (1998).
[42] H. Boukari, J. N. Shaumeyer, M. E. Briggs, and R. W. Gammon, Phys. Rev. A **41**, 2260 (1990).
[43] B. Zappoli, D. Bailly, Y. Garrabos, B. Le Neindre, P. Guenoun, and D. Beysens, Phys. Rev. A **41**, 2264 (1990).
[44] A. Onuki, H. Hao, and R. A. Ferrell, Phys. Rev. A **41**, 2256 (1990).
[45] A. Onuki and R. A. Ferrell, Physica A **164**, 245 (1990).
[46] A. Onuki, *Phase Transition Dynamics* (Cambridge University Press, Cambridge, England, 2002), p. 252.
[47] S. T. Boyd and J. Eraker (private communication).
[48] A. J. Liu and M. E. Fisher, Physica A **156**, 35 (1989).
[49] A. Onuki, Phys. Rev. A **35**, 5149 (1987).
[50] J. T. Stuart, in *Laminar Boundary Layers*, edited by L. Rosenhead (Oxford University Press, London, 1963); a more accessible reference to B_{cyl} is in R. E. Williams and R. G. Hussey, Phys. Fluids **15**, 2083 (1972).

Erratum: Shear thinning near the critical point of xenon [Phys. Rev. E 77, 041116 (2008)]

Robert F. Berg, Michael R. Moldover, Minwu Yao, and Gregory A. Zimmerli

(Received 13 February 2009; published 5 March 2009)

DOI: 10.1103/PhysRevE.79.039901 PACS number(s): 64.60.Ht, 83.10.Gr, 83.60.Df, 83.60.Fg, 99.10.Cd

A typographical error in a formula used to generate Tables VI–VIII resulted in incorrect tabulated values for $\omega\tau$ and $\dot{\gamma}_1\tau$ (the second and third columns). To obtain the correct values, multiply the original values by $(T/T_c-1)^{0.060}$, where $T_c=289.727$ K. For example, in Table VII the first value of $\omega\tau$ should be corrected from 7.0×10^{-5} to 4.3×10^{-5}. The error affects only Tables VI–VIII and the example given in the last sentence of Appendix C. The figures and the analysis are correct.